Polarized Fusion and Potential *in situ* Tests of Fuel Polarization Survival in a Tokamak Plasma

L. Baylor[6], A. Deur[1], N. Eidietis[2], W.W. Heidbrink[5], G.L. Jackson[2], J. Liu[3], M.M. Lowry[1], G.W. Miller [3,4], D. Pace[2], A.M. Sandorfi[1], S.P. Smith[2], S. Tafti [3], K. Wei [7], X. Wei[1] and X. Zheng[3]

[1] *Physics Division, Thomas Jefferson National Accelerator Facility, Newport News, VA, 93606 USA*
[2] *DIII-D National Fusion Facility, General Atomics, San Diego, CA 92186-9784, USA*
[3] *Department of Physics, University of Virginia, Charlottesville, VA 22904, USA*
[4] *Department of Radiology and Medical Imaging, University of Virginia, Charlottesville, VA 22908, USA*
[5] *Department of Physics and Astronomy, University of California, Irvine, CA 92697, USA*
[6] *Fusion Energy Division, Oak Ridge National Laboratory, Oak Ridge, TN 37831, USA*
[7] *Department of Physics, University of Connecticut, Storrs, CT 06269, USA*

E-mail: Sandorfi <sandorfi@JLab.org>, Smith <smithsp@fusion.gat.com>, Miller <gwm2n@virginia.edu>

ABSTRACT

The use of spin-polarized fusion fuels would provide a significant boost towards the ignition of a burning plasma. The cross section for the primary fusion fuel in a tokamak reactor, D+T → α+n, would be increased by a factor of 1.5 if the fuels were spin polarized parallel to the local field, rather than randomly oriented. Furthermore, our simulations show that additional non-linear gains in power would accompany this increase in large-scale machines such as ITER, due to increased alpha heating. The potential realization of such benefits rests on the crucial question of the survival of spin polarizations for periods comparable to the particle confinement time. During an initial peak of interest in such options during the 1980s, calculations predicted that polarizations could in fact survive a plasma environment, although concerns persisted regarding the cumulative impacts of wall recycling. In that era, the technical challenges of preparing and handling polarized materials prevented direct tests in research tokamaks and left the large scale fueling of a power reactor beyond reach. Over the last several decades, this situation has dramatically changed. Detailed simulations of the ITER plasma have predicted negligible wall recycling in a high-power reactor, and recent advances in laser-driven sources have projected the capability of producing nearly 100% polarized D and T in the quantities that would be needed to fuel a fusion reactor. What remains is the crucial step of verifying the expected gains from polarized fuel through an *in-situ* demonstration of polarization survival in a plasma. We outline

how such a measurement is now possible using the isospin-mirror reaction, $D+^3He \rightarrow \alpha+p$. The use of polarized ^3He avoids the complexities of handling tritium, while encompassing the same nuclear reaction spin-physics. Drawing upon advances in polarized material technologies, we evaluate two methods of delivering deuterium, using dynamically polarized Lithium-Deuteride (with deuteron vector polarization P_V^D of 70%) or frozen-spin Hydrogen-Deuteride (with P_V^D of 40%), together with a method of injecting optically-pumped ^3He (with 65% polarization). Once prepared for cryogenic injection, pellets of these material all have quite long polarization decay times (~ 6 minutes for LiD at 2 K, ~ 2 months for HD at 2 K, and ~3 days for ^3He at 77 K), all far greater than the duration of a plasma shot in a research tokamak such as DIII-D. Both species can be propelled from a single dedicated injection gun, with cooling stages at 2 K for polarized D, and ~80 K for polarized ^3He. Straight, vertical injection is preferred to maximize efficiency and plasma penetration. Signals of ~15 MeV protons provide an essentially background free signature of $D+^3He$ fusion. In a selection of shots with similar plasma characteristics, the expected ratios of yields from shots with fuel spins parallel and antiparallel range from 1.3 (HD + ^3He) to 1.6 (LiD + ^3He). Detailed tracking simulations for a high ion-temperature hydrogen plasma in the DIII-D tokamak confirm that this large signal should persist over a wide range of poloidal angles.

1. Introduction

The primary nuclear reaction for both magnetic and inertial confinement fusion machines is $D+T \rightarrow \alpha+n$. Both this reaction and its isospin-mirror process, $D+^3He \rightarrow \alpha+p$, are dominated at low energies by spin 3/2 *fusion* resonances that are just above the particle-decay thresholds in the compound nuclei ^5He and ^5Li, respectively [1, 2]. At keV energies such reactions are dominated by *s*-wave processes that involve no entrance-channel orbital angular momentum. Under these conditions it is obvious that a spin 1 deuteron and a spin ½ triton (or ^3He) will preferentially fuse into a spin 3/2 state when their spins are parallel, so an alignment of their spins would lead to an enhancement of the reaction cross section. While this had been known for decades [3], spin alignments are usually associated with low temperatures and the possibility that they could survive in a 10^8 Kelvin plasma for long enough to be useful seemed counter-intuitive. A paradigm shift came in 1982 with the seminal work of Kulsrud, Furth, Valeo and Goldhaber [4],

which predicted time scales for polarization loss in a plasma that were much longer than the characteristic fuel burn-up period. Since polarization-enhanced cross sections could potentially increase fusion efficiency, that paper led to considerable theoretical activity over the subsequent decade, see refs. [5, 6, 7, 8, 9, 10 and references therein].

During this period of initial excitement, a cost analysis was carried out by a group at Argonne National Lab in an attempt to project the impact of using polarized fuel in a future commercial DT fusion reactor [11]. The increase in reactivity was assumed to be a simple factor corresponding to fully polarized fuel (Section 2.2 below), but ignored the additional gains from increased alpha heating (see section 3). General assumptions were made regarding the costs of polarizing fuel by optical pumping. (We note that the subsequent advent of diode lasers has significantly decreased the cost of such an approach.) The costs of the magnets and the power plant as a whole were based on variations of the STARFIRE design. (It is worth noting that these assumed baseline reactor costs are about an order of magnitude lower than the current estimate for ITER.) Although the fractional changes found in that study were modest, a number of gains were noted in several key areas. Polarized fuel would decrease the cost of the current driver needed to establish ignition, would increase the lifetime of the first wall, would potentially allow for a lower field and a reduced plant size for the same power output, and would lower the operating cost per KW. While the cost balance has likely improved in the years since this initial analysis, their final assessment is undoubtedly valid – *polarized fuel is an option that can be applied if design conditions become difficult to achieve*. Given the challenges ahead, and a cost estimate for polarizing fuel that is an insignificant fraction of the total plant investment, the development of such a reserve is prudent, to say the least. This would require a technological development program with a comprehensive exploration of promising techniques together with in-plasma testing, preferably at an existing well-characterized facility [12].

During the 1980's, several polarization methods and many possible depolarization mechanisms were assessed, refs. [5-10]. However, in that era polarized nuclei were only available as gases or atomic beams of too low intensity to produce an observable signal, or as complex molecules containing high Z species whose large ionization energies would readily quench any plasma. In addition, there was no efficient means to deliver polarized fuel into a plasma, and so no practical way of testing the predictions of polarization survival. As a result, no experimental test was ever carried out and research activity in this area all but died out.

Over the last 30 years there have been key advances in the production of highly-polarized H and D, driven by nuclear and particle physics experiments [13, 14, 15], as well as in the production of highly-polarized ^{3}He gas for use both as a contrast agent in medical imaging [16, 17] and in high-energy spin physics. During the same period, ICF polymer shell technology has been extensively developed [18], and can now be used to contain polarized fuel (section 5). Finally, cryogenic injection guns have been demonstrated to convey pellets into the core of tokamak plasmas with high efficiencies [19]. The combination of these technologies that have matured since the original Kulsrud *et al* paper [4] can now be used to test the long-standing prediction of polarization survival, using the D+^{3}He $\rightarrow$ α+p reaction [20, 21]. As discussed below (section 2), the ^{5}He and ^{5}Li compound states in the $D+T \rightarrow \alpha+n$ and $D+^3He \rightarrow \alpha+p$ reactions have a nearly identical low-energy structure. Thus, polarization experiments can be conducted using the $D + {}^3He \rightarrow \alpha + p$ process, and the lessons learned directly applied to the planning of polarized $D + T \rightarrow \alpha + n$. (We note that while one might also consider polarized D+D reactions for such a test, the nuclear processes involved are in fact much more complicated. Current theoretical predictions for reaction rates with parallel deuteron spins span the range from a suppression by a factor of 10 to an enhancement of 2.5 over the unpolarized case [22]. While a study of polarized D+D has interesting nuclear structure ramifications, its use for quantifying polarization survival in a plasma presents many complications.)

Polarization survival is a key question, and in this paper we detail how such an experiment can be executed. The goals of the research that have led to the advances in polarized materials during the last decades, few mole samples with 10^5 to 10^8 sec lifetimes, are very mismatched to the requirements of fusion energy where ultimately several Kilo-moles per day would be needed, but with merely few second polarization lifetimes. Nonetheless, current technologies and existing facilities can be exploited in a cost-effective way for a test of polarization survival. While new laser-driven methods project the capability of feeding a reactor with polarized fuel (as discussed briefly in section 5.3), the crucial question of polarization survival must be addressed before investing in the development effort.

We continue with a review in the next section of the polarization-dependent reaction cross sections. In section 3 we report simulations of the additional impacts of polarized fuel from alpha heating in a large-scale tokamak, such as ITER. In section 4 we summarize expectations for depolarization rates from various possible loss mechanisms. The rest of the paper is devoted to a

detailed study of a viable polarization-survival test experiment using two sets of pellets, one containing a solid form of polarized deuterium (and two options are considered) and the other polarized ^{3}He gas, both introduced into the plasma of a tokamak by pellet injection. The general strategy and fuel preparation considerations are discussed in section 5. Simulations of the expected response are presented in section 6 for the particular example of the DIII-D tokamak, operated by General Atomics (GA) in San Diego. A companion paper contains a detailed discussion of detection strategies [23].

This paper outlines an experiment that cannot be executed without active participation from three very different disciplines – Fusion Energy Sciences (FES), Nuclear and Particle Physics (NP), and Radiological Imaging. Various details are included that may appear redundant to one group or another, but are included here for the sake of the broader audience. General concepts and preliminary progress on some aspects of this work have been reported in refs. [24, 12, 20, 21, 25].

2. Polarization-dependent fusion reactions

The polarization dependences and angular distributions of fusion cross sections are determined by the contributing levels in the fused compound nucleus. If only a single compound state contributes, polarization enhancements will be entirely determined by angular momentum and parity conservation. However, interfering transitions through neighboring levels could in principle complicate the problem. To address the magnitude of such effects we first consider the relevant energy range.

2.1 Fusion states at tokamak energies

Angle-integrated cross sections for the main fusion processes are shown in figure 1 as a function of their total center of mass (CM) kinetic energy [26], assuming no polarization in the entrance channels. While the D+T $\rightarrow$ α+n and D+^{3}He $\rightarrow$ α+p reactions become comparable above 250 keV, the former completely dominates at low energies. D+D reactions are intermediate at low energies but drop below other channels above 65 keV. A thermonuclear plasma contains a distribution of energies and the net fusion rate of two species are determined

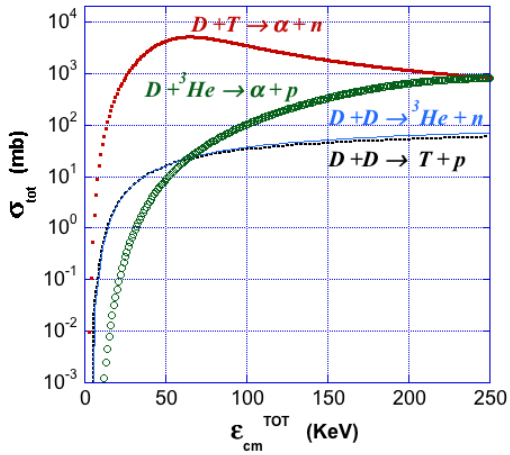

Figure 1. Total cross sections for relevant fusion reactions, from [26].

by their densities, N_1 (cm^{-3}) and N_2 (cm^{-3}), the effective plasma volume V (cm^3), and the cross section averaged over a Maxwell-Boltzmann velocity distribution <σ*v*> (cm^3/s) [27],

$$\langle \sigma v \rangle = \frac{4c}{\sqrt{2\pi M_r}(k_B T)^{3/2}} \int e^{-\varepsilon/k_B T} \varepsilon\, \sigma(\varepsilon)\, d\varepsilon \quad . \tag{1}$$

Here, ε is the total CM kinetic energy of the thermonuclear reaction, $M_r = m_1 m_2 / (m_1 + m_2)$ is the reduced mass and $k_B T$ is the ion temperature expressed in keV using Boltzmann's constant. (This assumes thermal distributions. When plasmas are heated with the injection of neutral beams, *eg.* ~80 keV at DIII-D, an additional rate component comes from the beam-plasma interactions at the higher CM energy.)

While Figure 1 is quite common in fusion literature, to appreciate the relevant energy ranges it is more instructive to examine the behavior of the fusion rate, <σv>. These determine the relevant energy ranges for the various channels. The running of eqn (1) is plotted in Figure 2 as a function of the upper limit of integration for different average ion temperatures, $k_B T$ [20]. For context, the highest temperature curve (18 keV) is the projected peak temperature for ITER and the next to highest (12 keV) is the expected average for the ITER plasma [28]. As is obvious from the figure, the fusion yield integrals are essentially saturated above about 50 keV for D+T, and above about 100 keV for D+^{3}He.

The ^{5}He and ^{5}Li compound states in the D+T→ α+n and D+^{3}He → α+p reactions are isospin-mirror nuclei and have a nearly identical low-energy structure. Both have a spin 3/2 capture resonance just above their particle decay thresholds, at 16.84 MeV in ^{5}He (50 keV above

the D+T threshold) and at 16.87 MeV in ^{5}Li (210 keV above the D+^{3}He threshold) [29]. Both compound nuclei have a gap of over 2.3 MeV between this J=3/2 *fusion* resonance and the next excited level, so that the only possible way higher states can contribute to fusion at tokamak energies is through the low-energy tails of broad states. Of the two reactions, D+^{3}He → α+p has the greater potential for encountering effects from interfering intermediate states, because of the higher energy of its spin 3/2 *fusion resonance* in ^{5}Li and the higher reach of its <σ*v*> integral.

The level spectrum of ^{5}Li is shown in Figure 3 [29]. The spin *3/2* second excited state at 16.9 MeV is the intermediate state of the ^{3}He+D *fusion* resonance. For fusion through this compound

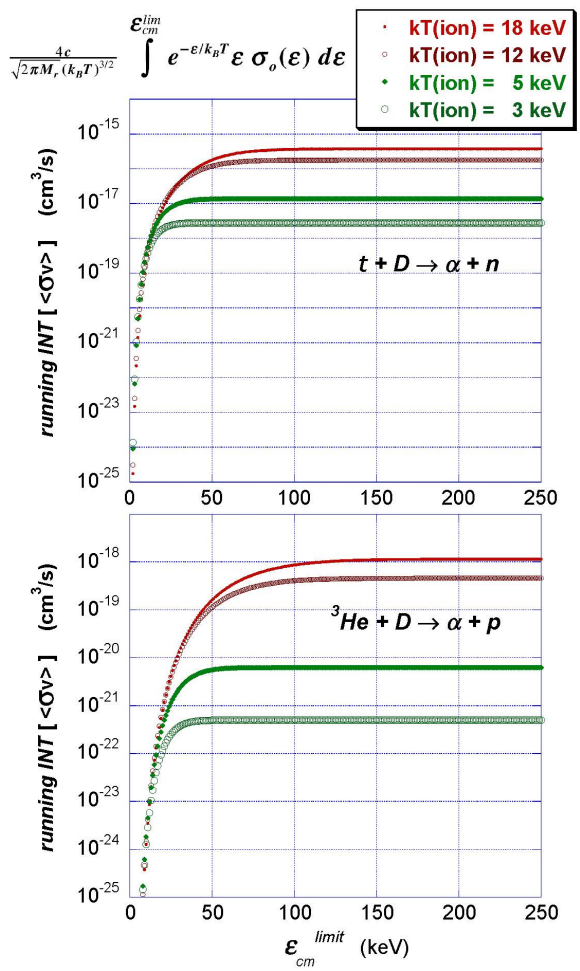

Figure 2. The running integral of <σ*v*> for *D+t* (top) and *D+^{3}He* fusion (bottom), plotted as a function of the upper limit of integration for four different average plasma ion temperatures; 18 keV and 12 keV are the projected peak and mean values for the ITER design [28].

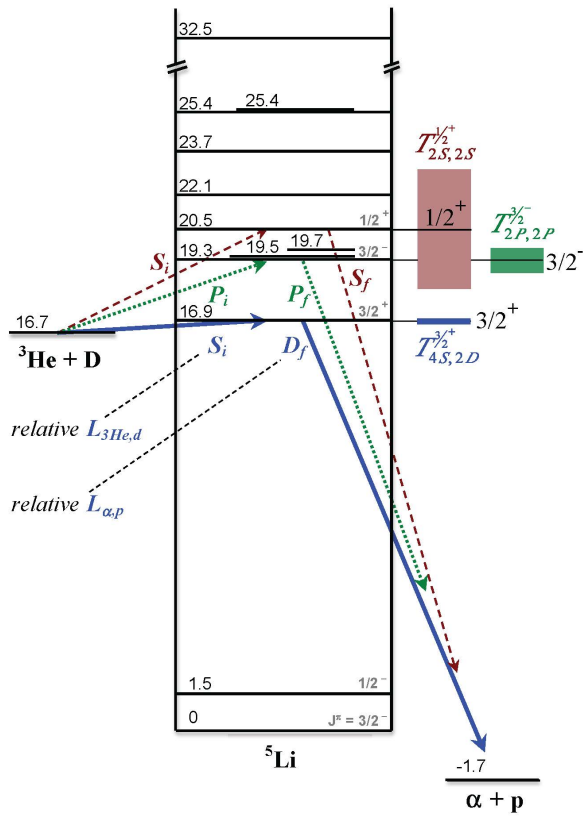

Figure 3. The energy level spectrum of ^{5}Li [29]. The widths of spin 1/2 and 3/2 states are schematically represented by the adjacent vertical bars.

state, angular momentum and parity conservation limit the orbital angular momentum to L_i=0 (S-wave) in the entrance channel, and to L_f =2 (D-wave) in the α+p final state. We follow the notation of Hale [30, 31] and of Lane and Thomas [32] and designate this transition amplitude as $T^{J^\pi}_{(2S_i+1)L_i,\,(2S_f+1)L_f} = T^{3/2^+}_{4S,\,2D}$. Fusion through higher spin states requires larger orbital angular momenta, which are greatly suppressed at tokamak plasma energies. There are only two other low-spin levels that might conceivably contribute, due to their very large widths, a $J^\pi=3/2^-$ state at 19.3 MeV above the ground state with a width of 1 MeV and a $1/2^+$ level at 20.5 MeV that has a 5 MeV width [29]. The corresponding transition amplitudes are designated $T^{3/2^-}_{2P,\,2p}$ and $T^{1/2^+}_{2S,\,2S}$, respectively. In this convention, the ***S***-matrix is just $2i\cdot\boldsymbol{T}$, and the total *unpolarized* cross section, averaged over initial spin states and summed over final ones, is

$$\sigma_0 = \frac{4\pi}{\left(k_D^{cm}\right)^2} \sum \frac{\left(2J_{^5Li}+1\right)}{\left(2J_D+1\right)\left(2J_{^3He}+1\right)} \left| T^{J^\pi}_{(2S_i+1)L_i,\,(2S_f+1)L_f} \right|^2 \quad . \tag{2}$$

Here the leading factor $k_D = P_D/\hbar$ is the deuteron wave-number (and P_D its momentum) in the center of mass.

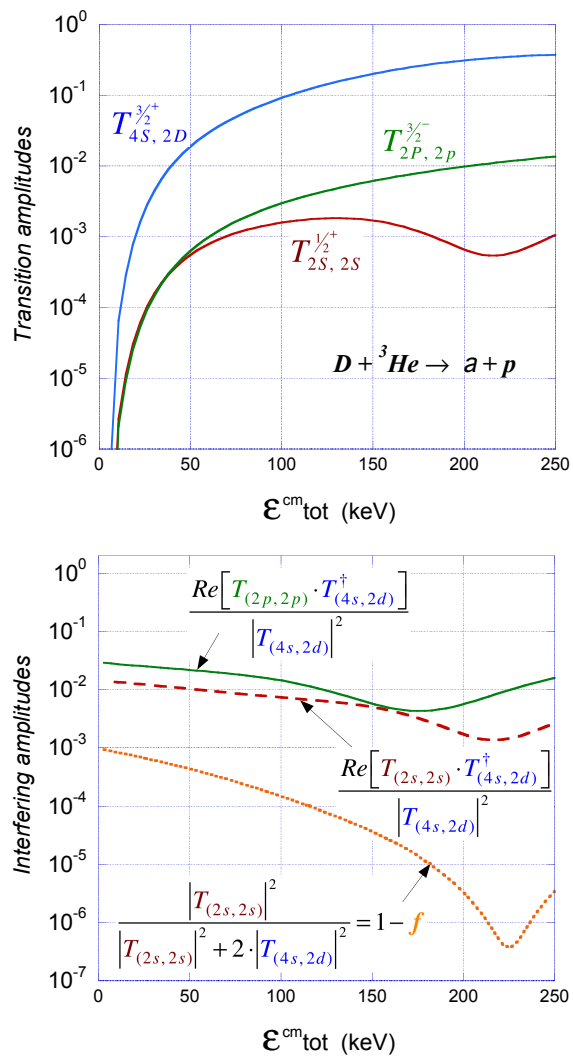

Figure 4. Transition amplitudes (dimensionless) for the $D + {}^3He \rightarrow \alpha + p$ reaction, determined from a recent *R-matrix* fit to all data up to 2006 [33] are shown in the upper panel. The leading terms contributing to the cross section from interference between the $T_{(4s,2d)}$ amplitude through the dominant $3/2^+$ compound state and $T_{(2p,2p)}$ and $T_{(2s,2s)}$ transitions through $3/2^-$ and $1/2^+$ states are plotted in the lower panel as solid and dashed curves, respectively. The dotted curve shows the dependence of (1-*f*), where *f* is the interference term discussed in [4].

An *R-matrix* analysis [33], fitting all recent polarization data, has been used to determine the transition amplitudes shown in the upper panel of Figure 4. In this energy range, the $T^{3/2^+}_{4S,\,2D}$ amplitude for transitions through the $J^{\pi}=3/2^+$ *fusion resonance* always dominates by more than an order of magnitude. The leading interference terms with the $T^{3/2^-}_{2P,\,2p}$ and $T^{1/2^+}_{2S,\,2S}$ transitions are plotted in the lower panel as the solid and dashed curves, respectively. (All other interference terms are at least an order of magnitude smaller.) For completeness, we have also plotted as a dotted curve the combination of amplitudes that determines the factor $\boldsymbol{f}$ considered by Kulsrud and collaborators [4]; $\boldsymbol{1-f}$ is plotted in Figure 4 since $\boldsymbol{f}$ is negligibly different from unity at all energies.

While recent polarization experiments have strongly affected the evaluation of the weaker transition amplitudes, there has been no real change to the total cross section, in which all interference terms drop out. A calculation of the total cross section with eq. (2) and the amplitudes of Figure 4 is indistinguishable from the 1992 evaluation of Bosch and Hale [26] that is plotted in Figure 1.

2.2 Angular dependence in Spin ½ + Spin 1 polarized reactions

The general formalism for calculating decay angular distributions in the $D+(^3He/T) \rightarrow \alpha +(p/n)$ reactions with a fully polarized entrance channel have been discussed in the literature for various intermediate-state spins [34, 35, 36, 37]. These follow from angular momentum and parity considerations. (As an illustration, a simple derivation for fusion from parallel and anti-parallel initial-state spin alignments is given in Appendix A.) In terms of the contributing amplitudes of figure 4, the final state cross section can be written as,

$$\frac{d\sigma}{d\Omega_{cm}} = \left(\frac{d\sigma}{d\Omega}\right)_0 \left\{ \begin{array}{l} 1 - \tfrac{1}{2} P_D^V P_{^3He}\left[1+(1-\boldsymbol{f})\right] \\ \\ + \tfrac{1}{2}\left[1-(1-\boldsymbol{f})\right]\cdot\left[3P_D^V P_{^3He}\sin^2\theta + \tfrac{1}{2}P_D^T\left(1-3\cos^2\theta\right)\right] \\ \\ - \dfrac{Re\left({}^{1/2^+}T_{2S,\,2S}\,{}^{3/2^+}T^{\dagger}_{4S,\,2D}\right)}{\left|{}^{3/2^+}T_{4S,\,2D}\right|^2}\left(P_D^V P_{^3He} - P_D^T\right)\left(1-3\cos^2\theta\right) \;+\; \ldots \end{array} \right\} . \qquad (3a)$$

Here the leading factor $\left(d\sigma/d\Omega\right)_0 = \frac{1}{4\pi}\sigma_0$ is the isotropic distribution determined by eq. (2) that would be observed in the absence of initial-state polarization. The factor $P_{^3He} = N_{+1/2} - N_{-1/2} \in$ [-1, +1] is the degree of ^{3}He polarization, determined by the sub-state population fractions relative to the tokamak magnetic field direction. Similarly, $P_D^V = (N_{+1} - N_{-1}) \in$ [-1, +1] is the deuteron vector polarization and $P_D^T = (N_{+1} + N_{-1} - 2N_0) \in$ [-2, +1] is the associated deuteron tensor polarization. The pitch (polar) angle θ is measured relative to the local magnetic field, as shown schematically at the top of figure 5. The leading interference terms all appear as the real parts of products of weaker amplitudes with the dominant $T^{3/2^+}_{4S,\,2D}$; one such term is shown explicitly in eq. (3a) as an example. For completeness, eq. (3a) also includes the combination of interfering amplitudes considered by Kulsrud *et al.* [4],

$$f = \frac{2\left|{}^{3/2^+}T_{4S,\,2D}\right|^2}{\left|{}^{1/2^+}T_{2S,\,2S}\right|^2 + 2\left|{}^{3/2^+}T_{4S,\,2D}\right|^2} \quad . \tag{3b}$$

As seen in the lower panel of figure 4, the leading interference terms provide less than a 3% correction to the angular distribution even at the lowest energies, and (***1-f***) is completely negligible at all energies. Thus, to an excellent approximation the differential cross section for the $D+^3He \rightarrow \alpha+p$ reaction, as well as for $D+t \rightarrow \alpha+n$ (with P_t replacing P_{3He}) where the interference terms are even smaller, may be simplified to,

$$\frac{d\sigma}{d\Omega_{cm}} = \left(\frac{d\sigma}{d\Omega}\right)_0 \left\{1 - \tfrac{1}{2}P_D^V P_{^3He} + \tfrac{1}{2}\left[3P_D^V P_{^3He}\sin^2\theta + \tfrac{1}{2}P_D^T\left(1 - 3\cos^2\theta\right)\right]\right\} \quad , \tag{4a}$$

and the Maxwell-averaged cross section becomes,

$$\begin{aligned}\left\langle d\sigma(\theta)v\right\rangle &= \tfrac{1}{4\pi}\left\langle\sigma_o v\right\rangle \cdot W(\theta) \\ &= \tfrac{1}{4\pi}\left\langle\sigma_o v\right\rangle \cdot \left\{1 - \tfrac{1}{2}P_d^V P_{^3He} + \tfrac{1}{2}\left[3P_d^V P_{^3He}\sin^2\theta + \tfrac{1}{2}P_d^T\left(1 - 3\cos^2\theta\right)\right]\right\} \quad .\end{aligned} \tag{4b}$$

Several observations are worth noting about the structure of eq. (4). The simple factorization in eq. (4b) holds as long as we neglect the interference terms, which as we have seen is an

excellent approximation. If the ^3He is unpolarized, the angular dependence of the differential cross section is modified from isotropy only by the tensor polarization of the deuteron. However, the angular factor of that term, $(1 - 3\cos^2\theta)$, integrates to zero in the total cross section so that the total reaction rate is not modified. (Nonetheless, as discussed in ref. [10, 12], this could potentially provide a measure of control over the direction of neutrons from D+T.) If the deuteron is unpolarized, the angular function $W(\theta)$ reduces to unity. Thus, the total fusion reaction rate differs from the unpolarized case only if *both* reacting species are polarized.

The angular distributions calculated from eq. (4) for full vector polarization $\{|\boldsymbol{P}^V_D| = 1, \boldsymbol{P}^T_D = 1$, and $|\boldsymbol{P}_{3He}| = 1\}$ are plotted in figure 5. For the case where the D and ^{3}He (or t) spins are both

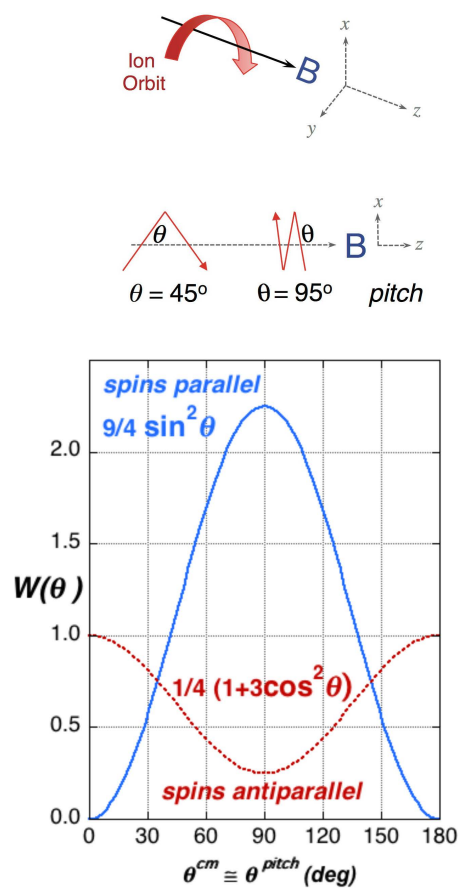

Figure 5. Ions follow helical paths around the local magnetic field lines. The *pitch* (polar) angles θ of reaction products are measured relative to the local field direction, as indicated schematically at the top of the figure. In the lower graph the angular distribution function $W(\theta)$ from eq. (4) has been evaluated for full vector polarization: $|\boldsymbol{P}^V_D| = 1$, $\boldsymbol{P}^T_D = 1$, and $|\boldsymbol{P}_{3He}| = 1$. The solid (blue) curve assumes parallel D and ^3He spins, while the dotted (red) curve is calculated for anti-parallel spin alignment. (A simple derivation of these distributions is given in Appendix A.)

parallel to the magnetic field, the angular function of eq. (4), $W(\theta)$, reduces to $9/4 \cdot \sin^2\theta$, which is plotted as the solid (blue) curve; for the corresponding case of anti-parallel spin alignment, $\{\boldsymbol{P^V_D} = \pm 1,\ \boldsymbol{P^T_D} = 1$, and $\boldsymbol{P_{3He}} = \mp 1\}$, $W(\theta)$ becomes $\frac{1}{4} \cdot (1 + 3\cos^2\theta)$ which is shown as the dotted (red) curve. The enhancement from parallel spin alignment is obvious. Integrating eq. (4) over all pitch (θ) and gyro-phase (ϕ) angles, determines the total reaction rate as,

$$\langle \sigma v \rangle = \langle \sigma_0 v \rangle \left\{ 1 + \tfrac{1}{2} \vec{P}^V_D \cdot \vec{P}_{^3He} \right\} \ , \tag{5}$$

where here we write the polarization factors as vectors, reflecting their range between [-1, 1]. Thus, if the spins of the reacting species are anti-parallel, the reaction rate is 1/2 of the unpolarized rate. But if the initial spins are parallel, the reaction rate is enhanced by a factor of 3/2, which is the original observation of Kulsrud [4].

3. Potential impacts for large-scale tokamaks

The fields and dimensions of high-power tokamaks such as ITER are designed to confine the alpha fusion products. Coulomb interactions of these alphas with electrons and with fuel ions raise the plasma temperature. At the expected ITER plasma energies of 10-20 keV [28], $\langle \sigma v \rangle$ increases roughly as the ion temperature squared, as shown in figure 6. This leads to an additional non-linear increase in the fusion power with polarized fuels beyond the simple polarization factors of eq. (5).

3.1 Steady-state power enhancement from polarized reactions

To project the equilibrium power output of an ITER-scale reactor fueled with polarized *D* and *T* we have solved the heat diffusion equation for the plasma temperature T,

$$\frac{\partial T}{\partial t} + \nabla \cdot \Gamma = S \ . \tag{6}$$

Here Γ is the heat flux density (related to $-\nabla \cdot T$) and S represents the *sources* (or *sinks*) of energy, $S = S_\alpha + S_{aux} + S_{rad}$, where $S_\alpha = n_D n_T \cdot \langle \sigma(T) v \rangle \cdot E_\alpha \cdot F$ represents the source from fusion

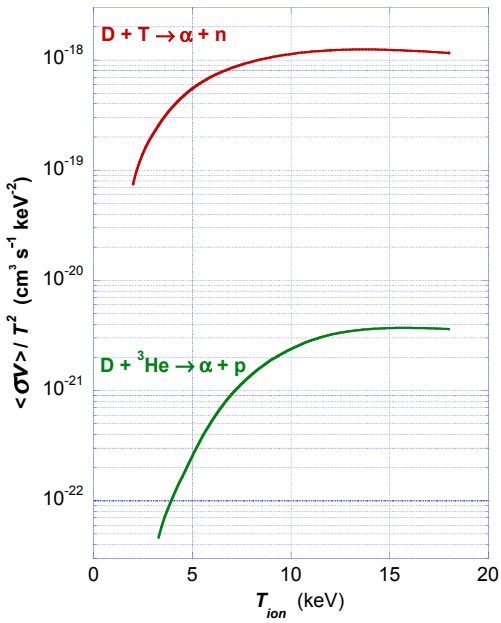

Figure 6. The reaction rate <σ*v*> divided by the square of the ion temperature for *D+T* (red) and *D+*^{3}*He* (green) fusion. For reference, the temperature of the ITER plasma is expected to span 10 –to- 18 keV [38].

reactions, with $F \in [1.0, 1.5]$ included here as a polarization enhancement factor, so that $F = 1.5$ corresponds to the fully polarized limit of eq (5). The parameter S_{aux} represents the external auxiliary heat applied to the plasma, and S_{rad} represents the heat lost from the plasma due to radiation. The code *TRANSP* [39] has been used to model the distributions of S_{aux} and S_{rad}. The heat flux perpendicular to the magnetic field lines arises from the helical motion of confined particles, smeared by coulomb scattering from electrons and ions (*classical transport*). Trapped particles experience a curvature drift with a coulomb smearing comparable to the dimensions of confined orbits (*neoclassical transport*), which is generally much larger [40, 41]. Larger still is the effect of *turbulence*, driven by electron and ion temperature and density gradients. In our simulations, the heat flux density has been taken as the sum of Γ(*neoclassical* and *classical*) + Γ (*turbulence*). For a steady-state condition, the heat flux must be matched to the source,

$$\Gamma_{neo} + \Gamma_{turb} = \int S\, dV \quad . \tag{7}$$

The calculation has been carried out for the ITER plasma, using the code *NEO* [42] to capture the effects of neoclassical and classical transport by numerically solving the drift-kinetic

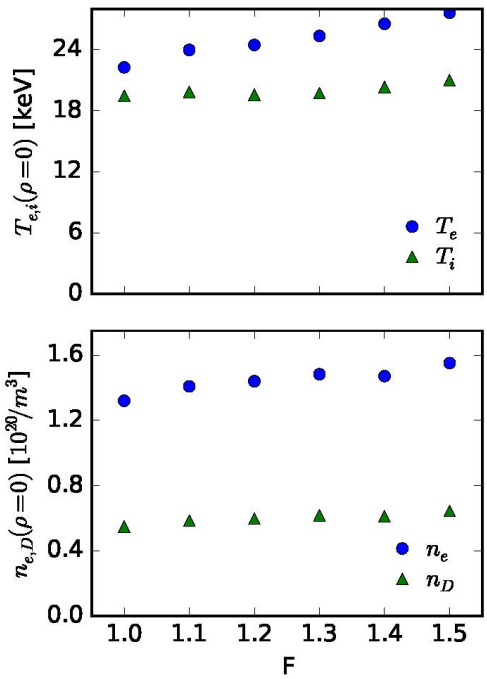

Figure 7. Expected core temperatures (top panel) and densities (bottom panel) of ions (triangles) and electrons (circles) for a steady-state condition in an ITER scale reactor, plotted for different values of the polarization enhancement factor $1.0 \leq F \leq 1.5$.

equation [43]. Turbulent flow has been simulated in a *trapped gyro-Landau-fluid* model using the code *TGLF* [44]. The steady-state condition of eq. (7) for ITER was obtained with the code *TGYRO* [45]. An ITER $Q = 12$ $D+T$ hybrid H-mode plasma [46] (with safety factor $q_{min} \sim 1.5$ at plasma radius $\rho = 0.3$) was used with 40 MW of externally supplied auxiliary power (P_{aux}) as the $F = 1$ starting point. The core electron density in this reference model plasma was ~ 1.3 x 10^{20} m^{-3}, accompanied by 100 MW of power in fusion alphas (P_α), so that $Q_\alpha = P_\alpha / P_{aux} = 2.5$ without fuel polarization. (The total fusion power will be 5 x P_α .) The resulting thermal ion and electron temperatures and densities in the plasma core are plotted in figure 7, as a function of the polarization enhancement factor F.

The predicted steady-state power from α heating transferred to ions and electrons is plotted in the top panel of figure 8. (A condensed summary of these simulations is given in ref. [25].) The sum of ion and electron contributions reflects the total alpha power. The associated power in fusion neutrons from $D+T \rightarrow \alpha+n$ is 4 times higher, and the total reactor power is 5 times the *total* values (diamond points) in figure 8. The lines below the points show the expected result

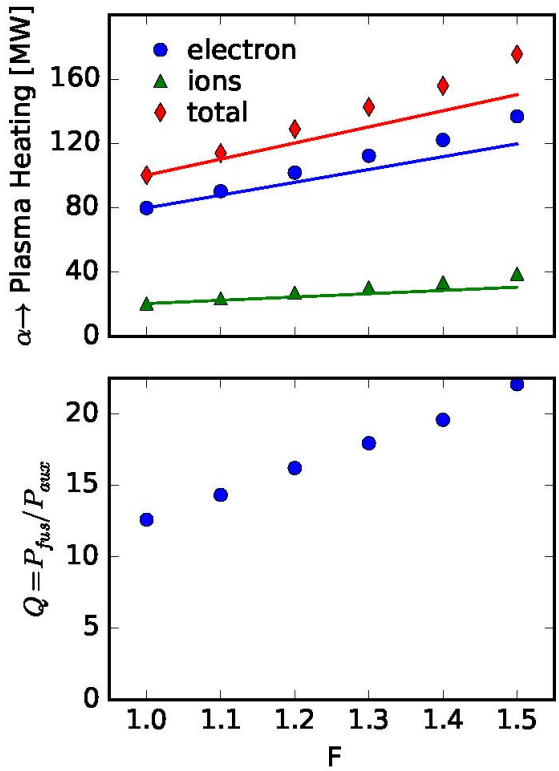

Figure 8. Predicted steady-state fusion heating levels in ions (triangles), electrons (circles) and their sum (diamonds), top panel, for increasing values of the polarization enhancement factor $1.0 \leq F \leq 1.5$. Lines show the expected behavior without alpha heating. The sum *total* reflects the power in fusion alphas. The ratio of fusion power (α+neutrons) to the 40 MW of auxiliary heating (P_{aux}) it plotted in the lower panel.

from just the polarization enhancement to the cross section of eq. (5); the excess reflects the increased alpha heating, which effectively shifts the CM reaction energy to a higher temperature where the cross section is larger. In this steady-state condition, the net effect of fully polarized fuel (F = 1.5) would be an increase in the fusion power by a factor of 1.8. This substantial enhancement is reflected in Q, the fusion energy gain factor (the ratio of the fusion power to the auxiliary heating), as shown in the bottom panel of figure 8.

3.2 Implications for magnetic fields in high power reactors

The fusion rate is the product of $\langle\sigma v\rangle$ with the fuel densities and the plasma volume. Another consequence of the T_{ion}^2 dependence evident in figure 6 can be seen by recasting the $D+T$ fusion rate as,

$$\begin{aligned} Rate &= N(D)\cdot N(T)\cdot\langle\sigma V\rangle\cdot V_{plasma} \\ &= \tfrac{1}{4\mu_0^2}\left[\frac{N(D)\cdot N(T)\cdot \mathrm{T}_{ion}^2}{B^4/4\mu_0^2}\right]\cdot B^4\cdot\frac{\langle\sigma V\rangle}{\mathrm{T}_{ion}^2}\cdot V_{pl} \quad = \tfrac{1}{4\mu_0^2}\left[\beta^2\right]\cdot B^4\cdot\frac{\langle\sigma V\rangle}{\mathrm{T}_{ion}^2}\cdot V_{pl} \end{aligned} \tag{8}$$

The ratio of plasma pressure to magnetic pressure, β in the above expression, is an approximate constant. In the temperature range for which $<\sigma v>/\mathrm{T}_{ion}^2$ is also approximately constant, the fusion rate becomes simply proportional to the fourth power of the tokamak field. Thus a 50% change in $<\sigma v>$ would allow a reduction in the magnetic field by 11%. This opens the possibility to use fuel polarization to compensate for field degradation of superconducting coils in existing machines. For future tokamaks, since plant costs scale roughly with B^2, fuel polarization could reduce costs by 25%, which represents a potentially huge savings.

4. Depolarization mechanisms in large and research-scale tokamaks

To be useful fuel polarization must survive, first as the polarized species undergo ionization, and then while they circulate as ions in the plasma. The impact of depolarization mechanisms in a large-scale (*eg.* ITER) machine versus a research tokamak can be very different.

4.1 Dilution from hyperfine splitting in partially ionized states following injection

The neutral ground states of all potential fusion fuels, either molecular TD or HD, as well as D_2 or T_2, or atomic ^{3}He, include two electrons paired in a zero-spin *1s* state having no net interaction with their nuclei. Upon injection, the nuclear spins immediately align along the local field. The magnetic field direction and magnitude changes are slow with respect to the precession frequency, which is the same order of magnitude as the cyclotron frequency, and hence adiabatic. A collision with circulating plasma electrons will quickly strip away the first atomic/molecular electron, and then the second on a time scale of ~10 μs later, which is still much longer than the precession time. In the interval before the nuclei are fully stripped and one electron is still bound, a hyperfine interaction (HFI) with the remaining bound electron will cause level mixing and a degree of dilution of the nuclear polarization. This interaction scales roughly with the cube of the nuclear charge, so the resulting dilution will be largest for ^{3}He. We discuss this issue here since, to the best of our knowledge, it has not been treated elsewhere. The

calculation for ^{3}He is outlined in Appendix B. The net fractional polarization loss as a function of magnetic field reduces to,

$$\frac{\Delta P}{P} = \tfrac{1}{2}\left[1 + \frac{4(\mu_e - \mu_{ion})^2}{A_{HFI}^2} B^2\right]^{-1} , \qquad (9)$$

where the magnetic moments of the spin ½ electron and ^{3}He are $\mu_e = (½)\gamma_e/2\pi$ = -14.013 GHz/tesla and $\mu_{ion} = (½)\gamma_{3He}/2\pi$ = -0.016 GHz/tesla, respectively. In ^{3}He where A_{HFI} = -8.66565 GHz, this results in 2% polarization loss at a field of 1.5 tesla. In a high field tokamak such as ITER, this effect will clearly be negligible. But for research-scale machines such as DIII-D a more careful estimate is necessary.

The magnetic fields in a tokamak are chiefly determined by the torus coils, where fields fall radially with 1/R. But the fields are modified by the poloidal coils and the plasma current itself. At DIII-D, the fields are obtained by solving the *Grad-Shafranov* equations for magneto-hydrodynamic (MHD) equilibria to determine the plasma current, using as constraints external magnetic field measurements and coil currents, together with current profiles from a number of diagnostics [47]. The magnitude of the DIII-D field in D_2 pellet shot S-96369 is plotted in figure 9. An illustration of hyperfine mixing effects in such fields is shown as the white curve, which gives the fractional loss in ^{3}He polarization calculated from eq. (9), assuming the magnetic fields along the Z=0 mid-plane. There the polarization loss ranges from 0.4% to 1.7%. The net effective polarization reduction must be weighted by the ^{3}He density in different field regions.

The expected density profile from the injection of a ^{3}He pellet has been modeled from measurements of shot S-96369, in which a D_2 pellet was injected into a deuterium plasma. An impurity level of fully-stripped carbon is also present (from the DIII-D graphite walls), and its density distribution is monitored with a *Charge-Exchange-Recombination* diagnostic [48]. A *Thompson Scattering* diagnostic [49] is used to monitor the electron density profile. Charge balance, $6\,N(C^{6+}) + N(D) = N(e)$, then determines the deuterium density (which includes deuterons injected as neutral beams). The difference in *N(D)* before and after the pellet injection is taken as representing the contribution of a pellet. The resulting distribution shown in figure 10 is assumed for a ^{3}He pellet injection.

The mean polarization loss from hyperfine mixing is calculated by summing over the full plasma region within the last closed field line, weighted by the particle density.

$$\left\langle \frac{\Delta P}{P} \right\rangle = \frac{\sum N\left({}^{3}He\right) \Delta P / P}{\sum N\left({}^{3}He\right)} \quad . \tag{10}$$

For ^{3}He, the mean effective polarization loss anticipated in DIII-D is $\langle \Delta P/P \rangle = 1.0\ \%$.

The strengths of the hyperfine interaction in other single-electron species that can occur during dissociation and ionization are listed in Table 1. The HFI strength is by far the largest in ^{3}He. Since the polarization correction from the latter is only 1%, hyperfine interactions in the others can be neglected in a DIII-D demonstration experiment (which is detailed in sections 5 and 6). Furthermore, since the polarization loss decreases with the square of the field, as in eq. (9), such HFI effects are expected to be irrelevant for ITER-scale machines that are designed to operate with about three times higher fields.

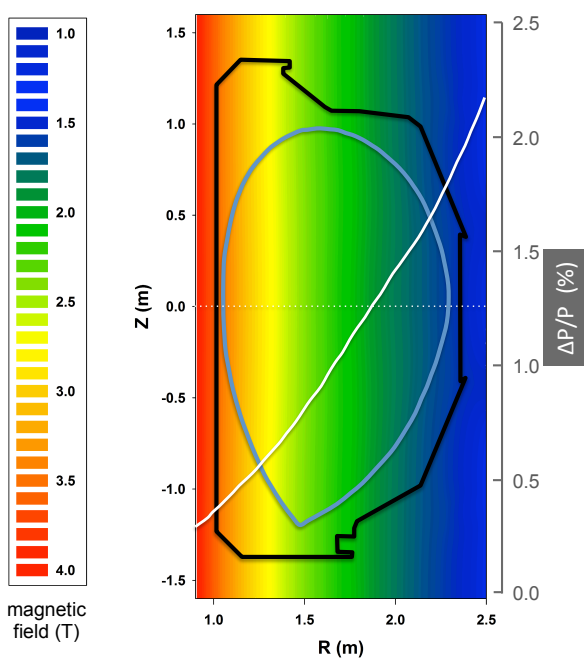

Figure 9. The magnitude of the DIII-D magnetic field in shot 96369 at T = 4575 ms, plotted in color contours with the scale legend to the left. The black polygon shows the relative position of the DIII-D vacuum chamber. The blue teardrop indicates the boundary of the last closed field line. The white curve, with its scale on the right, shows the fractional loss in ^{3}He polarization along the Z=0 mid-plane, due to hyperfine mixing in partially ionized $^{3}He^{+}$.

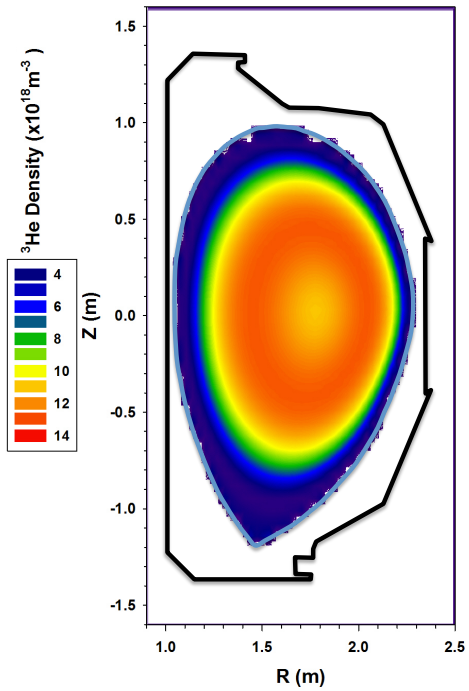

Figure 10. Fuel density following pellet injection, as deduced from DIII-D shot S-96369 at t = 4575 ms.

Table 1: Hyperfine interaction strengths in Single Electron Species

Species	A_{HFI} [GHz]	Reference
^{3}He+	-8. 665649867	[50]
H	+1.420405752	[51]
D	+0.327384353	[52]
T	+1.516701396	[53]
HD+	A_p =+0.925456 A_d =+0.142273	[54]

4.2 Polarization loss during the energy confinement period

A variety of possible depolarization mechanisms have been investigated theoretically. A summary of past work is given in [10] and the papers sited therein; recently, the issues have been revisited by Gatto [55]. There are essentially two mechanisms of concern that survive scrutiny, interactions with the tokamak walls and resonant interactions with plasma waves. The impact of these in large-scale (*eg.* ITER) machines versus research tokamaks can be very different.

Following injection, a small fraction of the fuel mass undergoes fusion in the tokamak core while most of the ions leave the plasma without undergoing a nuclear interaction. Upon reaching the walls, these ions pick up electrons and are neutralized. At the walls, there are several potential mechanisms that can, depending upon the structure and conditions of the wall material, lead to depolarization. However, the consequences of wall depolarization are moot in a high power ITER-scale reactor. ITER cannot be fueled by external gas jets (*gas puffing*) but must be fueled by pellets injected through the edge pedestal, because the Scrape-Off Layer (SOL) is expected to be almost opaque to neutrals from the walls [38, 56]. In ITER, particles leaving the plasma will be swept to the diverter by convection so that the recycling of fuel from the walls, and hence the dilution of the polarization in the core, is expected to be essentially insignificant.

This is not necessarily the case in a lower-power research tokamak. Potential wall-depolarization mechanisms have been discussed extensively in ref. [57], where low-Z, non-metallic materials were expected to be optimal. Fortuitously, the graphite walls of some research tokamaks, and DIII-D in particular, are well suited. Carbon has no conduction band, so that hyperfine interactions with polarized material are eliminated. However, the material is porous and excessive dwell times at the wall could compound the chance of encountering paramagnetic impurities. But this can be mitigated by the deposition of a thin (100 nm) layer of boron on the walls, which has been shown to dramatically increase confinement times [58, 59]. The reduced dwell-time on a *Boronized* wall, coupled with modest energy confinement times in research machines such as DIII-D (~0.2 s), is expected to be effective in keeping wall depolarization at a minimal level for a research program of spin-polarized fusion studies.

The electron and ion charges generate electromagnetic waves when boosted into the frame of the plasma current. A particular class, the Alfvén eigenmode, arises from the periodic boundary conditions of the tokamak geometry. (See ref. [60] for a recent overview.) When an ion's orbit is in phase with the eigenmode, their interaction can result in a larger displacement of the ion orbit, causing it to experience larger fluctuations in magnetic field. Several early papers [10, 61] speculated that excitation and amplification of these collective modes might be enhanced by the anisotropic decay angular distributions of figure 5, which could shorten depolarization times, particularly for tritium. Since they assumed many wall-plasma cycles, they concluded that triton depolarization could be significant. However, the main Alfvén eigenmodes are low frequency, compared to the cyclotron frequency, and $\Delta B/B$ during these orbits is on the order of 10^{-3}, which

is not expected to lead to significant polarization loss. In any case, as discussed above, wall recycling in an ITER-scale tokamak is not expected to be significant. Similarly, magnetohydrodynamic waves and microturbulence have frequencies too low to resonate with spin precession.

The plasma waves of concern are polarized collective emission in the ion cyclotron range of frequencies, which are of the same order as the D and ^{3}He Larmor precessions. Waves of this type, known as Ion Cyclotron Emission (ICE), are often driven unstable by anisotropic fast-ion populations from neutral beams or fusion products [62]. When ICE is unstable, many cyclotron harmonics are usually observed. Under different operating conditions, ICE is emitted from different regions in the plasma. In DIII-D for example, ICE tends to be emitted from the center of L-mode plasmas but often is restricted to the outer edge of H-mode plasmas [63]. Since the spin precession frequencies vary with magnetic field, which drops as 1/R in a tokamak (as in figure 9), if the ICE propagates throughout the plasma, an ICE harmonic may resonate with a D or ^{3}He spin-precession frequency somewhere in the plasma. In practice, the mode properties of a plasma are highly variable, and a plasma in which specific modes are suppressed can be developed, albeit with effort. In particular, plasmas with and without ICE should be created with polarized fuels to assess the relevance of this depolarization mechanism.

5. Fueling an *in situ* test in a research-scale tokamak

In this section we propose a measurement strategy for demonstrating fuel polarization survival in a research tokamak, using the DIII-D machine as a potential test bed. For the reasons discussed above, we choose $D+^3He \rightarrow \alpha+p$ as the test reaction, using separate sources of polarized D and polarized ^{3}He injected into a high-temperature (13 – 18 keV) *Quiescent H-mode* hydrogen plasma [64]. The resulting energetic protons will have large gyro-radii and will rapidly leave the plasma and be detected at several wall locations. Comparing proton yields from successive plasma shots with alternating fuel spin alignment maximizes the *signal* of polarization survival, as evident from eq (5). Suppressing some technical details, there are three key stages to such an experiment: the preparation of pellets of polarized D, preparing shells of polarized ^{3}He, each with sufficient spin lifetimes to make their loading into cryogenic injection guns practical,

and the synchronized injection into a high-temperature plasma with adequate shot reducibility. Below we discuss each of these in turn.

5.1 Polarized D pellet fueling

We outline three methods of preparing polarized D for tokamak injection. The first two are straight-forward adaptations of existing techniques that have been used to produce targets for Nuclear and Particle Physics (NP) experiments. Section 5.1.1 describes the use of Lithium-Deuteride as a carrier to deliver deuterium with 70% vector polarization. This would combine existing polarization, low-temperature and injection gun technologies, although their integration would necessitate a new engineering effort. Section 5.1.2 discusses the use of Hydrogen-Deuteride as the carrier to deliver deuterium with 40% vector polarization. This would require less of a construction project, mainly adapting existing equipment, but would involve many more stages and would become more of a labor effort.

The third polarization method (section 5.1.3), with investment and development, promises to produce intense sources of D (or T) with essentially 100 % polarization. In all methods, polarized material would be formed as cold pellets that could be injected with a cryogenic gun. In section 6, we conservatively model the proposed *Spin-Polarized-Fusion* (SPF) demonstration experiment assuming the conventional NP method of creating polarized D as discussed in 5.1.2, since this requires only the adaptation of equipment. Nonetheless, we include a condensed discussion of an *ultimate* method in section 5.1.3, to illustrate a path to a practical fueling scenario that could follow a successful confirmation of SPF.

5.1.1 Dynamically polarized $\boldsymbol{Li\vec{D}}$

Over the past decades, a variety of deuterated molecules have been used to create solid targets of polarized deuterium for nuclear and particle physics experiments [13, 14], the most commonly used being ammonia, ND_3. These utilize a *dynamic nuclear polarization* (DNP) process, in which molecular electrons are first polarized in a magnetic field at relatively low temperatures (~1K) and microwaves are then used to drive a hyperfine transition that transfers their spins to the deuterons. However, the extraneous high Z atomic species that accompany the polarized deuterium in these molecules generally have high ionization energies and radiation

losses that can act as sinks for power and can even potentially quench a plasma. For a SPF demonstration experiment, the most attractive of this class of material is Lithium-Deuteride, *Li D*. This material has reached the highest deuteron-vector polarizations reported, 70% [14]. Furthermore, not only does Lithium have relatively few electrons to alter the balance of the plasma, but it can in fact be a desirable addition, since Lithium injection is routinely used to improve wall conditions and mitigate *Edge Localized Modes* (ELMs) in tokamaks [65]. In terms of background fusion processes, only $^3He + ^6Li$ leads to protons with energies comparable to those from $D + ^3He$. These can be eliminated by using ^7LiD as the deuterium carrier, leaving ~15 MeV protons as a clean signature of $D + ^3He$ fusion. (Lithium is also polarized in the DNP process, but RF could be used to erase the ^7Li polarization just prior to tokamak injection. Thus, while background processes can contribute to the low-energy alpha yield, the polarization dependence would come solely from $D + ^3He$.)

Lithium-deuteride is a solid at room temperature and can readily be formed into mm-scale pellets suitable for a SPF study. The DNP process requires the introduction of a small fraction (~2%) of paramagnetic centers. These are introduced by radiation exposure at ~190 K, after which the material can be stored indefinitely at 77K. With DNP, the polarization grows with time as $P_o(1-e^{-t/T_1(D)})$, where $T_1(D)$ is the spin-relaxation time and P_o is a limit determined by the polarizing conditions (field, temperature, microwave spin-transfer efficiency, etc.). At 1 K and 5 tesla, deuteron vector polarizations saturate at about 50% in a few hours, and $T_1(D)$ is much longer than the typical duration of plasma shots at a research tokamak such as DIII-D (~ 20 s). Reaching the published maximum polarization of 70% would require DNP at 0.2 – 0.3 K and 6 - 8 tesla [66], with longer buildup times of 1 -to- 2 days. Thus, one could imagine an experiment that is *tuned* and refined at $P_V(D)$ = 50%, followed by a limited number of $P_V(D)$ = 70% shots requiring a longer spin buildup overhead. (Alternatively, multiple high-polarization ^7LiD pellets could be prepared simultaneously and stored for subsequent injection, although that would require another layer of equipment.)

The use of ^7LiD as the carrier for polarized deuterium would require a custom engineered polarizer, incorporating a DNP microwave circuit with RF coils that generate *Nuclear Magnetic Resonance* (NMR) signals for polarization monitoring and spin manipulations, coupled to a dedicated cryogenic injection gun, with a pellet handling system for multiple shots in 1 production cycle. The low operating temperatures of the polarizer would require either ^3He-^4He

dilution cooling to reach ~0.2 K, or a pumped ^{3}He system operating at ~ 0.3 K. (Neither of these are particularly challenging.) In the polarizer, the ^7LiD sample would need to be centered within a 6 – 8 tesla superconducting solenoid. While fringe fields from such a magnet might be of concern for plasma operations, since the bore of the solenoid could be small, this would require a relatively low inductance magnet that could be ramped down quickly (or even intentionally quenched) following the transfer of polarized pellets to the injection gun. The latter could operate at ~ 2K without noticeable loss in polarization over the short period (tens of seconds) preceding injection.

The number of deuterons in such ^{7}LiD pellets is listed in Table 2; 10^{20} is readily achievable.

5.1.2 Pellets of frozen-spin $\boldsymbol{H \cdot \vec{D}}$

Solid HD is not dynamically polarized, but rather is brought to a *frozen-spin state* at very high fields (15 tesla) and low temperatures (0.010 K). HD samples that have completed a polarizing cycle can be transferred out of these extreme conditions and maintained at modest fields (~0.1 tesla) and temperatures, with deuterium spin-relaxation decay times on the order of months at 2 K [15]. HD is a gas at room temperature and must be contained in order to pass through the multi-step polarizing process. Polymer shells, originally developed for *Inertial Confinement Fusion* (ICF), can provide an effective vessel.

We consider diffusing about 400 bar of molecular HD into 2 -to- 3 mm diameter *Glow-Discharge-Polymer* (GDP) shells, manufactured by General Atomics (GA) [18]. Polarizing HD requires removing heat at low temperatures. The much larger HD targets that have been used for NP experiments are cooled through contact with aluminum wires that thermally connect HD to a heat sink [15]. Alternatively, the cooling of SPF pellets can be achieved by adding ^{4}He gas, which at polarizing temperatures becomes a superfluid liquid. Such HD pellets can be cooled to a solid and transferred to a dilution refrigerator + superconducting magnet system where they can be polarized at ~10 mK and 15 tesla, using the NP techniques discussed in [15]. After the spins have become *frozen*, they can be cold transferred to another cryostat where radiofrequency (RF) excitations can be used to increase the deuteron polarization by transferring H spin to D [67]. A net deuteron vector-polarization of about 40% is expected. These pellets could then be shipped in a suitable cryostat to San Diego, loaded into a 2K cryogenic pellet injector and fired into the DIII-D tokamak with a cold, supersonic helium gas jet [19]. Apart from the filling of a thin-

walled GDP shell with high pressure HD (and ^{4}He), this stage just amounts to creating a small NP target with standard technology. The very long frozen-spin lifetime of such NP material allows the pellet polarization facilities and the tokamak to be separated by any distance, even thousands of km.

The characteristics of Glow-Discharge-Polymer (GDP) shells are discussed in Appendix C. When injecting these into a research tokamak it is necessary to keep the shell material to a minimum, so that the large ionization energy of the carbon atoms does not become a sink for power and quench the plasma. Thin-walled shells can be filled by controlling the temperature-dependent permeation rate. They are typically evacuated at room temperature by simply pumping on their storage container, and then filled with the gas of interest – in this case, a mixture of about 90% HD and 10% ^{4}He, the latter insuring the required thermal conductivity at the low polarizing temperatures. The characteristic permeation time constant (τ) depends linearly on shell dimensions, and inversely on both temperature and a temperature-dependent permeation coefficient, $\tau = Dw/(6K_pRT)$. Here D is the diameter of the shell and w the wall thickness, R is the gas constant, T is the temperature, and $K_p = K_0 \cdot exp(-\varepsilon_p/k_BT)$ is the permeation coefficient, with chemical activation energy ε_p (eV). (See Appendix C for further details.)

Permeation rates of ^{3}He, ^{4}He, and HD into 2 mm diameter GDP shells, with wall thicknesses

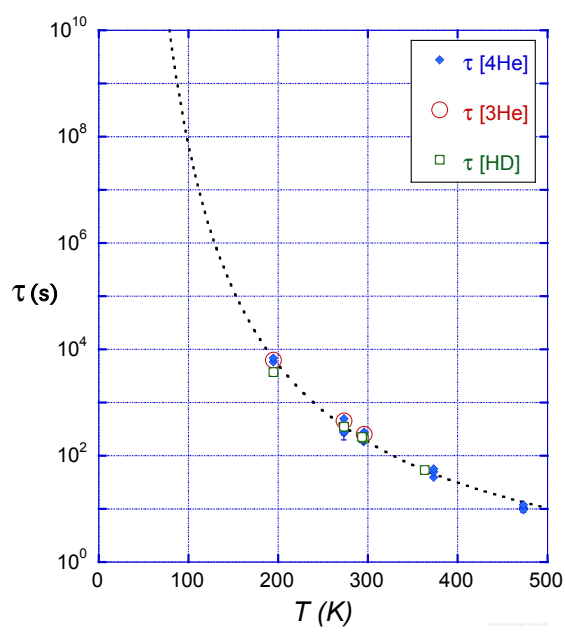

Figure 11. Permeation rates of ^{3}He, ^{4}He, and HD into 2 mm diameter GDP shells with wall thicknesses ranging from 16 μm to 29 μm. The dotted curve is a fit to the expected temperature dependence, as detailed in Appendix C.

varying between 16 μm and 29 μm, have been measured at JLab and results are plotted in figure 11 over a range of temperatures, together with a fit to the expected temperature dependence. (Details are given in Appendix C.) At elevated temperatures such as 150 C (423 K), gas quickly penetrated into the pellets ($\tau \sim 20$ s), but as the shell temperature is lowered the wall becomes completely sealed ($\tau \sim 300$ yr at 77 K).

In a typical filling scenario, one would increase the gas pressure on the outside of a GDP pellet in steps of 2/3 of the buckling pressure and wait 3 - 5 permeation time constants for the pressure across the pellet wall to equilibrate. By repeating this sequence, a thin-walled (~ 0.018 mm), 3 mm diameter pellet can be filled at ~425 K with 400 bar of HD (and 40 bar of ^{4}He) in about 12 hours. Cooling the permeation chamber to ~30 K reduces the pressure and increases τ to hundreds of years, completely sealing the pellet. At this point, the gas mixture outside of the pellets can be flushed and replaced with pure ^{4}He, keeping the pressure differential across the pellet wall well below the burst pressure of ~17 bar. Further cooling to the 16.6 K triple point of HD solidifies the HD on the inside wall of the pellet, and the ^{4}He pressure differential across the pellet wall becomes about 4 bar, which is still well below the expected buckling pressure of 6 bar. As the permeation chamber is cooled below 2.2 K the ^{4}He, both within and outside of the GDP shell, becomes superfluid and maintains efficient thermal contact with the walls of the chamber. The pellet then follows a routine NP target sequence until it is ready for transfer and shipment to the tokamak facility [15].

Such pellets would contain ~ 10^{20} polarized deuterons. As shown in Table 2, the accompanying unpolarized higher-Z material (Carbon from the GDP shell containing the HD) is much less than in the LiD scenario of Section 5.1.1, although a significant quantity of Hydrogen would be injected in this case.

5.1.3 High-flux laser-driven polarized $\vec{D}$

There is a significant potential for a new type of polarized source using molecular-physics techniques to reach unprecedented fluxes. In brief, deuterated (or tritiated) molecules can be Infra-Red (IR) laser-excited with circularly polarized light to a rotational state with unresolved hyperfine structure; these states then beat, and polarization is transferred between rotation and nuclear spin. This beating can be interrupted by rapidly applying a modest magnetic field, and

freezing the polarization on the deuteron (or triton). Polarized deuterons (or tritons) can then be separated by dissociating the molecules with an Ultra-Violet (UV) or visible laser. Since this can now be accomplished on the μs time scale, and no beam separation is necessary (as the polarization mechanism occurs within each excited molecule), it avoids the flux limitation of conventional (Stern-Gerlach type) methods that have been limited to low intensities to avoid collisional depolarization that occurs on the ms time scale in magnetic separation. Utilizing a recent revolution in high-powered lasers, the potential intensity gain over conventional atomic beam sources is about a factor of a million.

There are several versions of this general scheme [68, 69, 70, 71, 72]. We sketch one that is described in ref. [72] that can capitalize on new laser developments [73], and yield fully polarized sources of D, T or DT.

(i) As a source material, we consider a gaseous deuterated (and tritiated) formaldehyde, CDTO, CHDO or CD_2O, where only the hydrogen isotopes carry nuclear spin. The gas is expanded through a nozzle, and the cooling from expansion drives most of the molecules into their ground state with J(rotational) = 0, m_J = 0, ν(vibrational) = 0. The molecules exit the nozzle with a rather well-defined velocity of about 2 km/s.

(ii) The molecular beam then passes through two circularly polarized IR laser beams, fired perpendicular to the propagation direction. Through coherent Raman scattering (*Stimulated Raman Adiabatic Passage*, or STIRAP) they pump the molecule into a ro-vibrational excited state with two units of rotational angular momentum, $J = 2$ and $m_J = +2$.

(iii) The hyperfine (HF) interaction between the rotational angular momentum and the spins of the hydrogen isotopes splits the m_J levels. As the system evolves, the total angular momentum beats between rotational and nuclear spins, and the population of the fully nuclear polarized state ($m_J = -1$ for DT, or $m_J = -2$ for D_2) increases. Significant population (20%) in this fully polarized state is achieved after about 10 μs.

(iv) The beating rate between the nuclear and orbital spins allows time for the molecular beam to travel from the gas expansion nozzle to a region with a modest field (a few milli-tesla) that stops the hyperfine beating at a point when the population in the state with full nuclear polarization is large.

(v) Within the field region, another IR laser transition selects the hyperfine level with full nuclear polarization and pumps it to a $J = 1$, $m_J = +1$ state of DT (or to $J = 0$ for D_2) . This state is exclusively photo-dissociated with a high-resolution visible laser, tuned so that only the state with full nuclear polarization has sufficient energy to dissociate. The dissociating laser line can be chosen to break the bond of interest, so as to yield CO + DT (or COH +D, *etc.*), depending on the source gas.

(vi) The dissociation region ends within a larger field magnet (~1 tesla), which prevents hyperfine beating in the separated isotopic hydrogen atoms between electrons and their polarized nuclei. The molecular rotational angular momentum J =1, created by the IR excitations in the previous step, also aligns the molecular bonds, since the orbital angular momentum J and the bonds are always perpendicular. As a result, the polarized fragments will be emitted with a center of mass angular distribution that is highly peaked perpendicular to the initial nozzle-expansion momentum. After dissociation, the polarized DT (or D) carry almost all of the kinetic energy. If the preceding stages are arranged vertically, the dissociated CO (or COH) fragments will continue to drift downward, while the polarized hydrogen-like atoms emerge highly peaked horizontally.

The result of the previous steps is an intense source of highly polarized DT molecules (or D atoms) with ~100% nuclear polarizations [72]. It would be relatively straight forward to collect and freeze these in open-ended capsules cooled to ~ 2 K, which could then be transferred to a cryogenic pellet injector.

Most of these steps have already been demonstrated, although only at relatively low powers. Commercial table-top, tunable, narrow band-width lasers should produce polarized fluxes of 10^{21} s^{-1}. Industrial scale lasers could exceed fluxes of 10^{22} s^{-1} with nearly 100% polarization [73]. With such capabilities, scenarios for fueling a tokamak reactor with polarized fuel become realistic. Nonetheless, as with any new technique that jumps previous boundaries by many orders of magnitude, focused research and development will be necessary to demonstrate the predicted flux scaling. The driving factor for such research is a demonstration of polarization survival in a realistic plasma.

5.2 Polarized ^{3}He pellet fueling

Hybrid spin-exchange optical pumping (SEOP) can be used to polarize ^{3}He [16]. With this technique, a glass bulb containing pressurized ^{3}He, together with small amounts of Rubidium and Potassium (~ 10^{14}/cc) and Nitrogen (~0.7 %), is heated to about 475 K (200 C) to vaporize the alkalis. The Rb vapor is polarized with 795 nm circularly polarized light from diode lasers, and collisions with the alkali atoms transfer polarization to the ^{3}He, usually in the sequence Rb $\rightarrow$ K $\rightarrow$ ^{3}He. After several hours the ^{3}He polarization has saturated (at about 65% in the polarizer used for the studies reported below [17], although higher levels have been reported by other groups [74]), after which the temperature of the polarizing cell is lowered. The vapor pressures

of Rb and K drop rapidly with temperature, so that at 293 K (20 C) their concentrations are less than $10^{10}/cm^3$ and essentially negligible. At this point, the ^3He can be extracted from the polarizing cell and used to fill a GDP pellet, with the same general procedures described above in the filling of HD shells. The key difference here is that the ^3He must be laser polarized *first* to avoid vaporizing the GDP shell, the polarization must survive permeation of the GDP wall material and, after the temperature has been lowered to seal the wall, the polarization decay time within the pellet must be sufficient to allow for transfer to a pellet gun and injection into a tokamak. The GDP pellet fabrication process is known to leave free radicals within the material of the shell wall. This potentially exposes polarized ^3He to trapped paramagnetic impurities, which can contribute to depolarization. Once inside the pellet, experience with NP targets has shown that scattering from confining walls can be an important limitation to the ^3He polarization lifetime [75]. Such wall relaxation effects are material dependent, and need to be investigated because of the high surface/volume ratio inherent to the small ICF pellets.

5.2.1 Polarization losses during pellet permeation from MRI

The permeation and polarization survival characteristics of ^3He in GDP shells have been studied using 2 mm diameter GDP pellets supplied by General Atomics [76]. A clinical *Magnetic Resonance Imaging* (MRI) scanner with a nominal field strength of 1.5 tesla at the University of Virginia (UVa) [17] has been used to track the filling process by generating 3D polarization images of GDP shells during permeation. We outline the highlights of these studies here; extensive details are described in refs. [77, 78]. Measurements were performed in borosilicate glass assemblies which ended in a tube with an inner diameter of 3 mm that contained a GDP pellet, as shown in figure 12. The glass tube was connected to a valved buffer volume between the gas inlet port and the entrance to the section containing a pellet. The latter was surrounded by a pair of saddle-shaped RF coils tuned to the ^3He resonance frequency. After evacuating all of the glass sections, and the GDP shells in the process, the buffer volume was filled with room-temperature polarized ^3He gas while isolated from the pellet region, and then rolled into the scanner so that the pellet and the RF coils reached the isocenter of the MRI magnet system. Only then was the buffer valve opened, flooding the GDP pellet region with polarized gas. In this way the permeation process could be actively imaged.

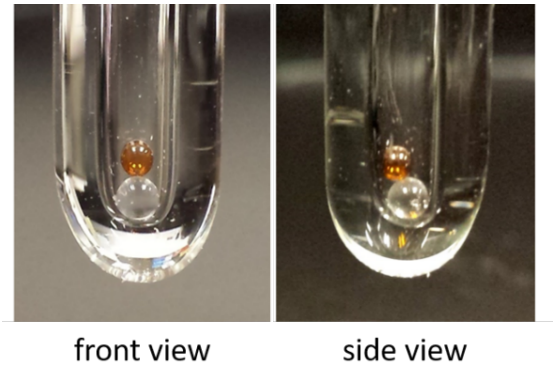

Figure 12. The typical placement of a 2 mm diameter GDP pellet (which appears amber in these photographs) above a Pyrex bead within a 3 mm inside-diameter (ID) tube for permeation imaging.

Imaging results from a tube containing an 18-micron thick wall X 1.8 mm diameter GDP pellet are shown in Figure 13. The MRI was performed using a *chemical shift imaging* pulse sequence, which provides both spatial and spectral information. Frequency shifts induced by the presence of the Pyrex bead allow the spins inside and outside the GDP shell to be tracked separately. (Details of the MRI process are given in Appendix D.) Figure 13 shows 2D images at a vertical slice containing the GDP pellet of figure 12. (The intrinsic resolution is 0.5 mm X 0.5 mm. The images have been interpolated to finer pixel size using standard MR image processing algorithms. The original pixelated images are reported in ref. [77, 78].) The top row shows the total signal at each location versus time, obtained by summing the signal magnitude over the entire frequency spectrum originating from each voxel. The overlaid circle indicates the location of the pellet. This signal increases at the pellet location for about the first 8 minutes, corresponding to ~2 permeation time constants at room temperature, and then begins to fall.

The frequency-resolved polarization densities from spins inside and outside the GDP shell are plotted in the middle and bottom panels of figure 13, respectively. The sequence of images in the bottom panel reveal the decay (*longitudinal relaxation*) of spins in the glass tube, with exponential time constant T_1 . The images in the middle panel clearly show the action of two

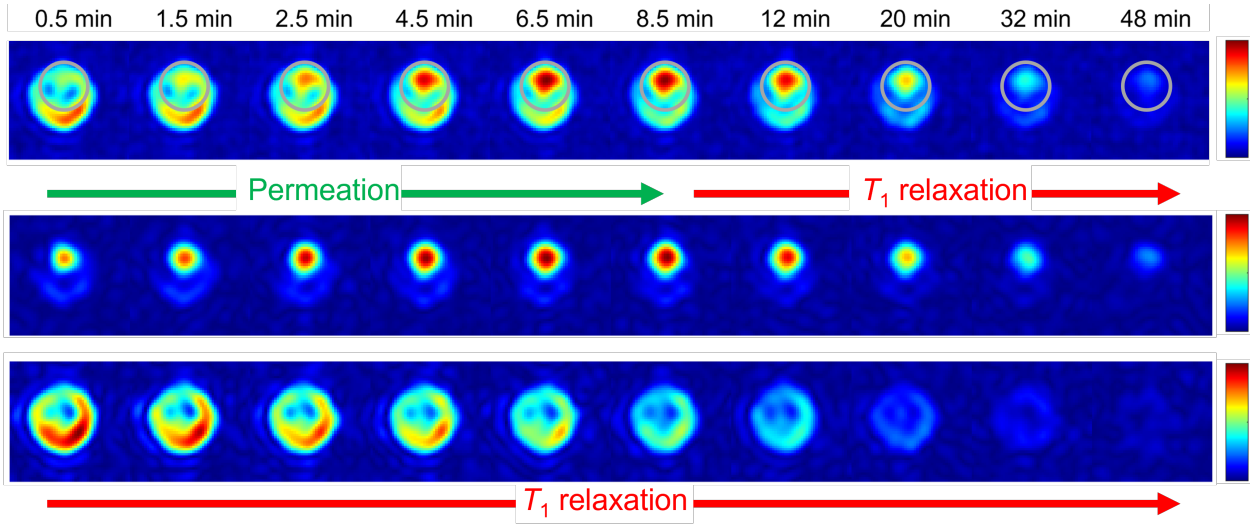

Figure 13. Imaging results obtained during the permeation of polarized ^{3}He into a GDP pellet with 18-µm wall thickness and 1.8 mm diameter. Top row: concatenated image series showing the total ^{3}He signal at the indicated times after the initial introduction of gas into the sampling tube of figure 12. A red color indicates higher polarization density. Circles indicate the position of the pellet. Frequency-resolved signals originating from ^{3}He spins located inside and outside the pellet are shown in the middle and bottom panels, respectively.

time-dependent processes, permeation of spins into the pellet and their room-temperature relaxation. The former has been measured independently for the GDP pellet of figure 13, τ_{perp} = 3.78 ±0.07 min. (following Appendix C). The latter is dominated by the T_1 relaxation of gas in the tube, T_1^{tube} = 27 ±1 min. for the tube of figure 12, since at room temperature ^{3}He is continually exchanged across the pellet wall from an essentially infinite spin reservoir outside the pellet.

A comparison of the ^{3}He polarization density within the pellet, integrated over the frequency shifted *intra-pellet* peak, and the spin density outside the pellet gives the fractional loss in polarization during the permeation of the pellet wall, 22 ±1 % for the 18 µm-wall GDP pellet of figure 12. The loss in pellets with thicker walls increases roughly in proportion to the increased permeation time [77, 78], when filled at the same temperature. The pellet material is known to contain potentially depolarizing free radicals and the time that the ^{3}He spends within the GDP material is the crucial factor. However, since the permeation time is a strong function of temperature (*eg.* figure C1 of Appendix C), it should be possible to keep polarization losses in thicker walled pellets to a minimum by filling them at an elevated temperature.

5.2.2 Spin lifetime of encapsulated ^{3}He at 77 K

Once a pellet is filled with polarized ^{3}He, the temperature must be lowered to seal the GDP shell (as in figure 11). To be useful, the lifetime of the encapsulated spins must then be long enough to allow transfer of such polarized pellets to a gun for tokamak injection.

Further imaging measurements were carried out, using the same arrangement as described above. A 17 μm-wall X 1.8 mm diameter GDP shell, positioned on top of a 3 mm solid glass bead (similar to figure 12), was positioned at the isocenter of the MRI scanner, after which the valve separating the ^{3}He buffer volume was opened to the pellet region of the tube. An initial 2D image is shown in the left panel of figure 14, taken ~1 min. after the tube was flooded with polarized gas. The solid glass bead appears as the opaque sphere at the bottom. Above this is the GDP pellet in the early stage of permeation. After about 2 permeation time constants, the end of the tube containing the pellet was immersed in liquid N_2. The gas within the tube provided a thermal coupling between the GDP shell and the tube walls, which quickly lowered the pellet temperature to 77 K, sealing the pellet wall. Then, ~15 min. after the initial introduction of ^{3}He, the tube was evacuated, reducing the pressure outside the GDP shell to a few mb., which was sufficient to maintain thermal contact with the glass tube wall at 77 K, while contributing negligible extra-pellet signal to subsequent imaging. A 2D image taken ~ 2 min later (middle panel of figure 14) shows polarized ^{3}He confined to the pellet. Another image, with the same

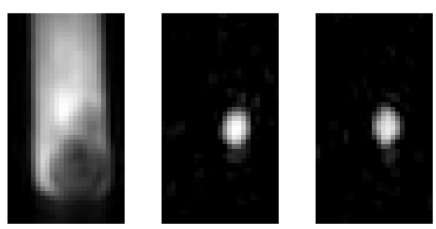

Figure 14. LEFT PANEL: A 2D MRI scan of a 17 μm-wall X 1.8 mm ∅ GDP pellet on top of a 3 mm ∅ solid glass bead, within a glass tube similar to that of figure 12, is shown just after the tube was flooded with polarized gas. The white regions indicate the presence of polarized ^{3}He. After this image was obtained, the gas was allowed to permeate the GDP pellet for ~ 10 min. before cooling to 77 K by immersing the tube in liquid N_2, which sealed the pellet wall. About 5 min. later, the gas outside the pellet was evacuated. MIDDLE PANEL: A 2D MRI scan taken at 77 K, ~15 min after the initial introduction of polarized ^{3}He, and just after removing the ^{3}He gas outside the pellet. RIGHT PANEL: A 2D MRI scan taken at 77 K, 6 hours after removing the gas outside the GDP pellet. The intensity scale of the right panel figure is the same as that in the middle panel.

intensity scale, taken 6 hours later is shown in the right panel, from which it is clear that very little polarization decay has occurred since the ^{3}He was sealed within the pellet.

The longitudinal relaxation of the spins within the GDP pellet at 77 K was tracked with a simplified NMR measurement at regular intervals over a span of 10 hours. Imaging was not necessary since the pellet was the only source of ^{3}He polarization. Each RF excitation flips a small fraction of spins, and so consumes hyperpolarized magnetization. Thus, each RF burst decremented the ^{3}He polarization, although by less than 0.5%. Even though each such loss is small, taken together they are not negligible compared with the longitudinal relaxation that occurred over the duration of the experiment. Nonetheless, correcting for them is straight-forward [77, 78]. The RF-loss-corrected measurements are shown in figure 15. Fitting these data to an exponential decay gives a longitudinal relaxation time of the ^{3}He polarization in the GDP pellet as T_1 ~ 3 days at 77 K. For comparison, the result without the RF-loss correction would have been ~ 2 days [77, 78].

A 77 K spin relaxation $T_1(^3He)$ of ~3 days is extraordinarily long for a confining cell with such a high surface-to-volume ratio. This is likely associated with the extremely smooth surface of these shells that have been produced for ICF applications. Fortuitously, such long $T_1(^3He)$ times provide a manageable window for loading a cryogenic tokamak injection gun.

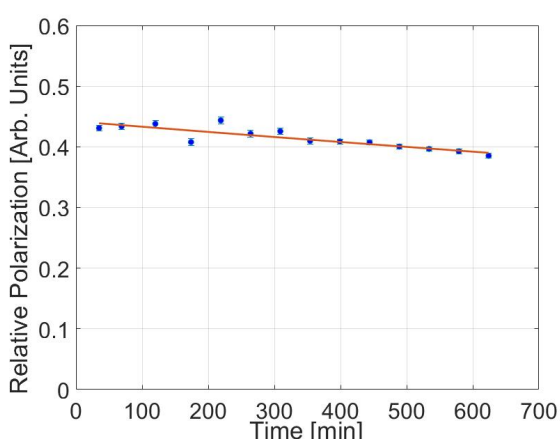

Figure 15. Measurements of ^{3}He spin relaxation inside a GDP pellet, after cooling to liquid N_2 . The data points show the signal versus time since reaching 77 K, after correcting for RF-induced polarization losses during the measurements. The fit (red curve) corresponds to a relaxation time of T_1 ~ 3 days.

5.2.3 ^{3}He-fuel pellet preparation for a SPF demonstration experiment

The results in the previous sections demonstrate that polarized ^{3}He can be encapsulated in GDP shells. The magnetic resonance imaging techniques discussed above provide a method of monitoring the expected polarization loss as hyperpolarized ^{3}He is permeated through the walls of GDP pellets. As discussed in Appendix D, to actively monitor permeation in mm-scale pellets with sufficient spatial resolution, the geometry of these loss measurements must be restricted to small gas volumes, and these have relatively short room-temperature polarization relaxation times ($T_1 \sim ½$ hr). In the measurements discussed in section 5.2.1, this resulted in the decay of about half of the available polarization before the GDP shell could reach its full pressure. GDP pellets intended for tokamak injection would be prepared in a substantially larger volume of about a liter, with an expected T_1 on the order of 125 hr [79], while in parallel, polarization loss during permeation would be monitored for a small sampling of the GDP shells using an MRI system similar to that described above.

The fractional polarization loss is roughly proportional to the time the ^{3}He gas spends within pellet wall material, which depends both on the wall thickness and the permeation temperature. We illustrate the production of GDP shells with 18 μm wall thickness for tokamak injection, using the model calculations of ref. [77, 78].

The polarizer used for the measurements discussed in the previous sections was limited by the requirements of its original medical imaging application. For a tokamak demonstration experiment an optimized SEOP ^{3}He polarizer can be constructed. ^{3}He polarizations up to 85% have been demonstrated, using frequency-narrowed diode laser pumping of volumes of about a liter [74]. For these calculations we assume a polarization performance of 80% at 25 atm, in a cell with T_1 of 125 hr at room temperature [79]. For 18 μm wall x 1.8 mm diameter shells (*eg.* the GDP pellet of figure 13), the buckling pressure is 9.2 atm. Permeation could take place in a series of steps, where the outside-inside pressure difference is incremented by 2/3 of the buckling pressure at each step, ie. 6 atm. This is illustrated as the blue dashed curve in figure 16. Maintaining the pressure for 4 permeation time constants (= 4 x 3.8 min at 295 K for this shell) fills a pellet to 98.2% of the exterior pressure at each step (the blue dashed-dot curve), so that the interior pressure reaches 24 atm in about an hour at 295 K. The expected polarization growth profile for such a pellet, including the polarization loss during permeation, is shown as the solid

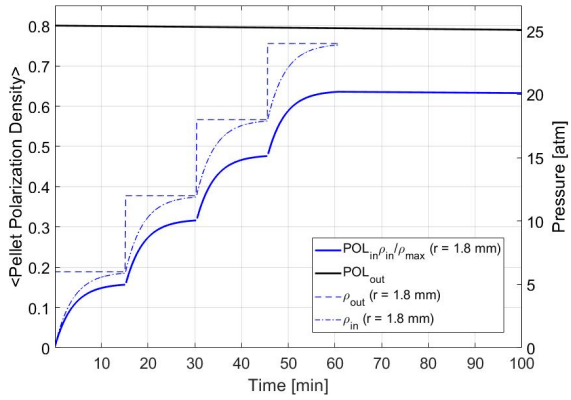

Figure 16. Expected ^{3}He polarization growth as tokamak shells are filled to 24 atm at 295 K in steps to avoid implosion, with the exterior and interior pressures (ρ) illustrated by the dashed and dashed-dot curves (as in the legend). The model of ref. [77, 78] is used to account for polarization losses during permeation of GDP pellets with 1.8 μm thick walls, and diameters of 1.8 mm. The mean polarization density is shown as the solid blue curve.

blue curve in figure 16, and reaches about 65%. With the short permeation time, spins are constantly being exchanged across the pellet wall. Since the spin reservoir is huge compared to the volume of the pellet, the net T_1 of gas inside the pellet is essentially the same as that of the reservoir. A filled pellet can be cooled to 77 K with liquid nitrogen, at which point the pellet wall is sealed, the internal T_1 becomes ~ 3 days (figure 15), and the internal pressure drops to 6.2 atm. Since this is substantially below the burst pressure of 27.6 atm, the exterior pressure can safely be lowered to the few mbar needed to maintain thermal contact with the 77 K container walls. At this point the pellet would be ready for transfer to a 77 K gun in preparation for tokamak injection.

The 1.8 mm outside-diameter (OD) GDP shells modeled in figure 16 contain ~0.2 x 10^{19} atoms of polarized ^{3}He. Larger shells with 3 mm OD and the same wall thickness could be filled in a similar manner to ~1 x 10^{19}. This is about an order of magnitude lower than the number of polarized deuterons that could be injected (Table 2), but this could partly be compensated by simultaneously firing multiple ^{3}He pellets. The latter is not so great a complication since the ^{3}He pellet injector only need operate at 77 K. In any case, the reaction rate is proportional to the product $N(D)$ x $N(^3He)$, as in eqn (8), and so it is not essential that the two densities be identical.

Polarization loss during permeation limits the ultimate ^{3}He spin that can be encapsulated. However, the GDP pellet production process leaves free radicals within the shell material. Those

used in the measurements discussed above were stored in air prior to shipment to JLab, and in the presence of ambient light that catalyzes reactions with oxygen. Recent work has revealed the formation of O-H hydroxyl bond structures on the surface under these conditions [80]. The paramagnetic character of these O-H bonds is a likely source of depolarization. GDP pellets made specifically for ^{3}He encapsulation could reduce this loss simply with an improved storage environment prior to usage.

5.3 Cryogenic injection of Polarized pellets

An SPF demonstration measurement must be initiated by the injection of polarized D pellets, either as GDP shells containing solid HD or as solid ^{7}LiD pellets, followed quickly (within tens of ms) by polarized ^{3}He in GDP shells. Deuterium pellets can be injected at ~2 K, while ^{3}He would be injected at ~77 K. For a practical realization of such an experiment, it is likely that a dedicated injection gun would be constructed to operate at 2K, or below. Since reaching low temperatures requires a 70 K -to- 90 K radiation shield, cooled either with liquid N_2, boil-off liquid helium or by an intermediate cooling stage from a closed-circuit cryo-cooler, a single injection gun could be engineered to accommodate the injection of both polarized species. The gun would need to incorporate an internal magnetic field to maintain pellet polarizations, and a field of about 0.1 tesla would be sufficient. At 2 K and 0.1 tesla, the measured $T_1(D)$ polarization decay time is about 2 months for frozen-spin *HD* [15]. For *LiD*, $T_1(D)$ is proportional to $e^{2\mu_e B/kT}$, where μ_e is the magnetic moment of the paramagnetic electrons used in the DNP process. Scaling down existing higher field data [66], a $T_1(D)$ of about 6 minutes is expected at 2 K and 0.1 tesla. For polarized ^{3}He at 77 K, $T_1(^3He)$ is ~3 days, as in figure 15. Although the latter result was measured at 1.5 tesla, the field dependence of $T_1(^3He)$ is very weak and 0.1 tesla is much larger than is typically used in NP experiments [81]. While *LiD* has the most restrictions of these polarized species, its T_1 is still much longer than the time needed to transfer a pellet from an adjacent polarizer to an injection gun (~1s), ramp down the polarizing magnet (~10 s), ramp up the DIII-D torus field (~7 s), and fire the cryogun (~1 ms).

In existing solid (unpolarized) D_2 pellet guns, samples are propelled from the 4K barrel of a cryo-gun to the tokamak by room temperature helium gas [19]. Downstream of the ~ 0.5 m long gun barrel, room temperature guide tubes, with staggered differential pumping to remove the

propellant gas, provide a vacuum envelop for the flight trajectory to the tokamak with a telescoping inner diameter to avoid contacting the pellet during its ~ms flight.

The guide tube following this new 2 K gun could remain at room temperature since it has no direct contact with the pellet and the radiation from the walls during the ~ms transit time is very small. However, to minimize polarization loss, cold helium gas should be used to propel polarized pellets, and a triggered flash evaporation of liquid helium could be a possible source of cold pressurized propellent. The injection of polarized ^{3}He pellets from a barrel cooled by the 70 K -to- 90 K stage could follow a similar parallel path, with multiple tubes to guide several of the lower density ^{3}He shells merging into the same guide tube.

Pellet injection from various points in the DIII-D tokamak has been studied, and vertical injection (designated *V+1* in ref. [19]) appears to be the most attractive for SPF. The pellet velocities are the highest, consistent with essentially no wall collisions along the straight guide tube, giving the pellet a high probability of entering the tokamak intact. (Experience with the injection of polymer spheres on DIII-D has shown that shells with gas payloads are in fact more likely to survive the flight down the guide tube without fracturing, compared with shells containing loose solid material, which presumably reacts to the impulse of acceleration [82]. Nonetheless, in the case of HD pellets, the polarized material would be frozen onto the inside surface of the GDP shells, and so is not expected to be susceptible to this problem.) The *V+1* trajectory is on the High Field Side (HFS) of the plasma distribution and much less of the pellet mass is ejected, leading to a higher fueling efficiency and deposition depth, compared with Low Field Side (LFS) injection. Finally, while all pellets injected into H-mode plasmas trigger ELMs, regardless of their injection point, those ELMs induced by HFS and *V+1* injection are qualitatively no different from the normal background ELMs.

The D and ^{3}He polarizations must be maintained by a magnetic field throughout their flight path to the outer edge of the Tokamak. For deuterium, typically a few hundred gauss is sufficient; for ^{3}He, even 25 gauss will preserve the in-flight polarization. Such fields can be generated by a solenoid winding wrapped around the guide tube, with a tapered wire density that decreases as the tube enters the fringe field of the tokamak. While injection velocities are typically ~500 -to- 1000 m/s, this and/or some tumbling motion down the guide tube are significantly slower than the Larmor frequencies of either D or ^{3}He. As a result, the D and ^{3}He spin vectors will simply follow the net local field as the tokamak fringe field rises and the guide

tube field falls. (See ref. [15] for an example of spins transferred through different field orientations without loss of polarization.) Once inside the hydrogen plasma, the spins will align along the local magnetic field.

The anti-parallel spin configuration can be prepared within the cryo-gun, using an RF transition (an *Adiabatic Fast Passage*, or AFP) to flip the sub-state population so that the spin of the ^{3}He (or the D, but not both) is aligned against the local magnetic field [67].

5.4 Extraneous material accompanying polarized pellets

Injected ^{3}He shells (S. 5.2), and either option for polarized Deuterium, ^{7}LiD (S. 5.1.1) or HD (S. 5.1.2), would introduce extra material into the plasma, The quantities are summarized in the last four columns of Table 2. The LiD pellets introduce the most higher-Z material, although at Z=3 Lithium has the least detrimental impact. Furthermore, since separate Lithium injection is routinely used to suppress ELMs, both species in a LiD pellet injection could have a beneficial role. The HD shells have the lowest amounts of higher-Z material, coming from their GDP casing, although these pellets introduce appreciable quantities of Hydrogen that could lower the average ion temperature. However, the high-T_{ion} Quiescent H-mode plasma required for this measurement would be generated by injecting 80 keV neutral H-beams against a counter-rotating ion current, as has been done in ref [64] with D beams and plasmas. The inevitable cooling from the extraneous material can be compensated by neutral-beam injection timed to immediately follow a polarized fuel injection.

Table 2: Achievable number densities, particles per fuel pellet in units of 10^{19}, are listed with their degree of ^{3}He or D polarizations for different pellet diameters. For deuterons, both vector and tensor polarizations are given. The quantities of extraneous accompanying material from the deuteron carrier and/or the shell material are also tabulated. The different polarization processes are discussed in Section 5.1.1 for ^{7}LiD, in Section 5.1.2 for HD, and in Section 5.2 for ^{3}He.

			$^3\vec{He}$		$\vec{D}$			*extraneous material*			
carrier	***pellet ∅ (mm)***	***shell***	**# $^3\vec{He}$ (x 10^{19})**	**$P(^3He)$ (%)**	**# $\vec{D}$ (x 10^{19})**	**$P_v(D)$ (%)**	**$P_T(D)$ (%)**	**# ^4He (x 10^{19})**	**# H (x 10^{19})**	**# C (x 10^{19})**	**# ^7Li (x 10^{19})**
^{7}Li D	1.0	—			3.2	70	41				3.2
^{7}Li D	1.5	—			10.7	70	41				10.7
HD	1.8	GDP			2.1	40	12	0.2	3.1	0.9	
HD	3.0	GDP			9.8	40	12	1.0	12.6	2.8	
^{3}He	1.8	GDP	0.18	65					1.0	0.9	
^{3}He	3.0	GDP	0.85	65					2.8	2.4	

6. Simulations of polarization enhancement in DIII-D

The signal of polarization survival is a spin-dependent change in the fusion rate, and the largest changes can be revealed by comparing charged fusion product yields from successive plasma shots in which D and ^{3}He are injected with their spins alternatively parallel and anti-parallel (as evident in figure 5). Assuming the anticipated polarizations of D and ^{3}He as summarized in Table 2, $P_V(D) = 70\%$ with a ^{7}LiD carrier (S 5.1.1), or $P_V(D) = 40\%$ with an HD carrier (S 5.1.2), and $P(^3He) = 65\%$ (S 5.2), the simple expectation from eq. (5), ignoring details of the DIII-D *acceptance* (the efficiency for protons to reach specific detectors at the wall from different locations within the plasma), would be

$$\frac{\langle \sigma^{par} v \rangle}{\langle \sigma^{anti} v \rangle} = 1.59 \ , \ \text{from } ^7\text{LiD} + ^3\text{He pellets,}$$

$$\frac{\langle \sigma^{par} v \rangle}{\langle \sigma^{anti} v \rangle} = 1.30 \ , \ \text{from HD} + ^3\text{He pellets .} \tag{11}$$

To account for the DIII-D acceptance, we have conservatively modeled the lesser of these two, the scenario expected from the injection of HD and ^{3}He. This is described in the subsequent sections. There are several options for monitoring these ratios of fusion products at the plasma-facing wall. Both Fast Ion Loss Detectors [83], and Silicon surface barrier detectors have been successfully used at DIII-D [84].

6.1 Plasma Parameters for Modeling and Simulation

We model a DIII-D experiment designed as a hydrogen plasma, heated by hydrogen neutral beam injection, in a plasma configuration that produces the highest possible ion temperature in a fairly repeatable plasma. The proposed experiment to demonstrate the survivability of polarized fuel (i.e., fuel remaining polarized long enough for a fusion reaction to take place) involves a set of plasma characteristics that have not been combined into a single shot on DIII-D. As such,

initial modeling from past shots begins with plasma characteristics that are similar to those desired and then scales parameters as necessary to predict the outcome of a polarized fuel experiment. The modeling involves a calculation of the instantaneous fusion rate and then an orbit-following calculation of the charged fusion products. To model the fusion rate, data from a solid D_2 pellet injection into a D plasma, DIII-D shot 96369, has been used. This is simulated with the power balance code ONETWO [85], in which the injected pellet is treated as providing a ^{3}He *impurity*, scaling ion energies and cross sections to represent D + ^{3}He reactions. The effective number of each species present in this simulated condition is about 6 x 10^{20}. The fusion product orbits are then evaluated using a magnetic equilibrium that is calculated for the reference plasma by the EFIT code [47], which processes various plasma diagnostic measurements to determine the resulting flux surfaces and electric field profiles. (Here, the orbit trajectories are calculated without electric field profiles and collisional scattering, both of which generate only small corrections for the high energy D+^{3}He fusion products.) The resulting charged fusion product flux along the plasma-facing wall can then be compared between the parallel alignment and the anti-parallel orientations of initial D and ^{3}He spins.

Figure 17 shows the constructed temperature profiles used to produce the largest absolute fusion rate. In DIII-D, peak central ion temperatures of 15 keV have been achieved in a Quiescent H-mode deuterium plasma following deuterium pellet injection [64]; this is used as the peak value modeled. Fusion rates have been scaled by the ratio of D+^{3}He -to- D+D cross

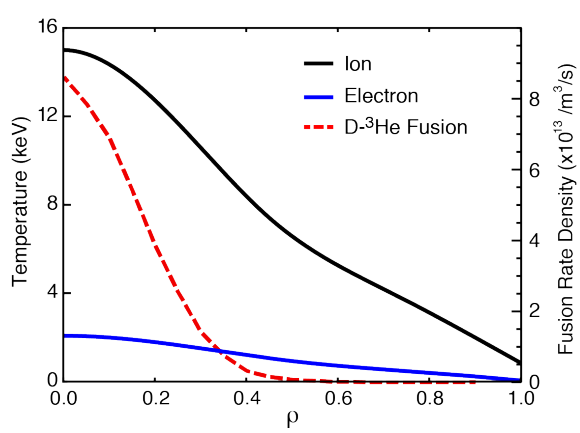

Figure 17. Ion and electron temperature profiles, with their scale on the left, for the modeled case featuring the largest absolute fusion rate. These profiles have been modified based on original data from shot 96369, scaling the peak ion temperature from 5 keV up to 15 keV. The resulting fusion rate is plotted as the dashed red line, with scale on the right. The horizontal axis, ρ, represents the normalized value of the square root of the toroidal magnetic flux.

sections, and the resulting D+^{3}He fusion rate is shown as the red dashed curve in Figure 17, where the horizontal axis, ρ, is the effective radial coordinate - the normalized value of the square root of the toroidal magnetic flux. The fusion rate is strongly peaked in the core, as expected given the sensitive dependence of the fusion cross section on ion temperature.

6.2 Tracking fusion products in DIII-D

The fusion rate density of figure 17 is converted to a discretized function of major radius and vertical position and used to source the appropriate number of $\alpha + p$ fusion products. This provides the number of particles originating at each specific location; that number is then divided amongst the possible birth pitch and gyrophase angles, weighting their relative number by the polarized angular distributions of eq. (4). The orbits of the α and p fusion products are then tracked through the DIII-D magnetic field until they strike the plasma-facing wall. Details of the orbit modeling are provided in Appendix E.

The left panel of Figure 18 shows the geometry of the tokamak as a cross-section of major radius and elevation. The right-panel plots two 14.7 MeV proton orbits. One proton originates at

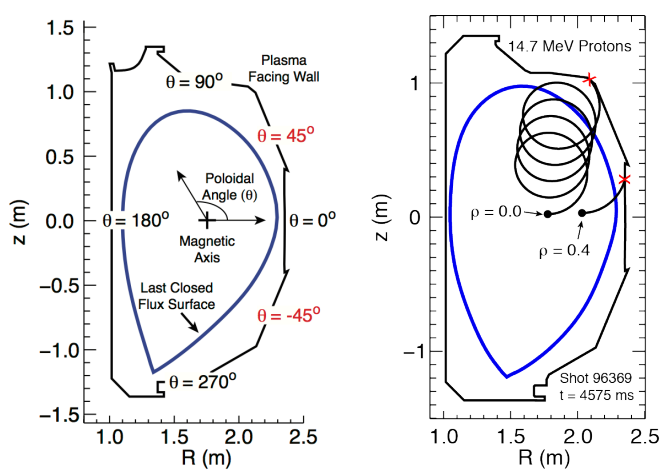

Figure 18. (Left) Tokamak geometry for the orbit modeling of D+^{3}He charged fusion products. Poloidal angles are defined relative to the midplane. (Right) Examples of toroidal orbits of 14.7 MeV protons, projected onto a 2D slice through the torus field, and striking different parts of the DIII-D wall.

the magnetic axis and the other at ρ = 0.4 which, as is evident in Figure 17, is about the approximate radial extent of significant fusion activity. Both protons have the same birth gyrophase for this example, and they reach the vessel wall at quite different poloidal positions.

The calculation of the wall strike positions for the full distribution of charged fusion products, integrated over pitch and gyrophase angles at birth, provides the poloidal profile of arriving particle flux. This is shown in figure 19 for protons (top panel) and alphas (bottom panel), for parallel and anti-parallel D and ^{3}He spin as the blue and red histograms, respectively. This simulation has assumed 40% deuteron vector polarization, with an accompanying 12% tensor polarization (from HD filled shells, as in S 5.1.1), and 65% ^{3}He polarization. As expected from eqn. (11), there is more yield when the initial D and ^{3}He spins are parallel (blue histograms). The patterns have a relative maximum above the 0^0 mid-plane (at positive poloidal angles), reflecting

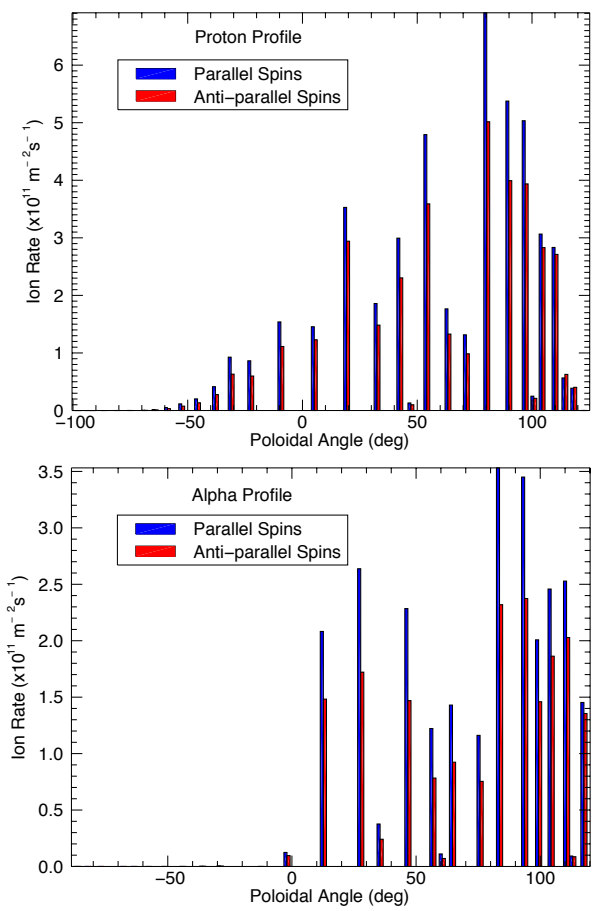

Figure 19. Yield of protons (top) and alphas (bottom), integrated over birth pitch and gyrophase angles, as a function of poloidal angle at the DIII-D vacuum wall, for initially parallel (blue) and anti-parallel (red) D and ^{3}He spin orientations.

the characteristic *acceptance* of DIII-D when its magnets are energized so that the total magnetic field rotates counter-clockwise when viewed from above. (The pattern is reflection-symmetric with field, so that the relative maximum would appear below the mid-plane if the energizing currents were reversed. The latter is assumed in the simulations of ref. [23].)

The ratios of expected yields from DIII-D shots with anti-parallel and parallel D and ^{3}He initial spin alignments are shown in figure 20 for protons (top) and alphas (bottom) at different locations along the plasma-facing wall of the DIII-D vacuum vessel. The strong signal of eq. (11) is maintained over a large range of wall locations. Although the departure of the ratio from

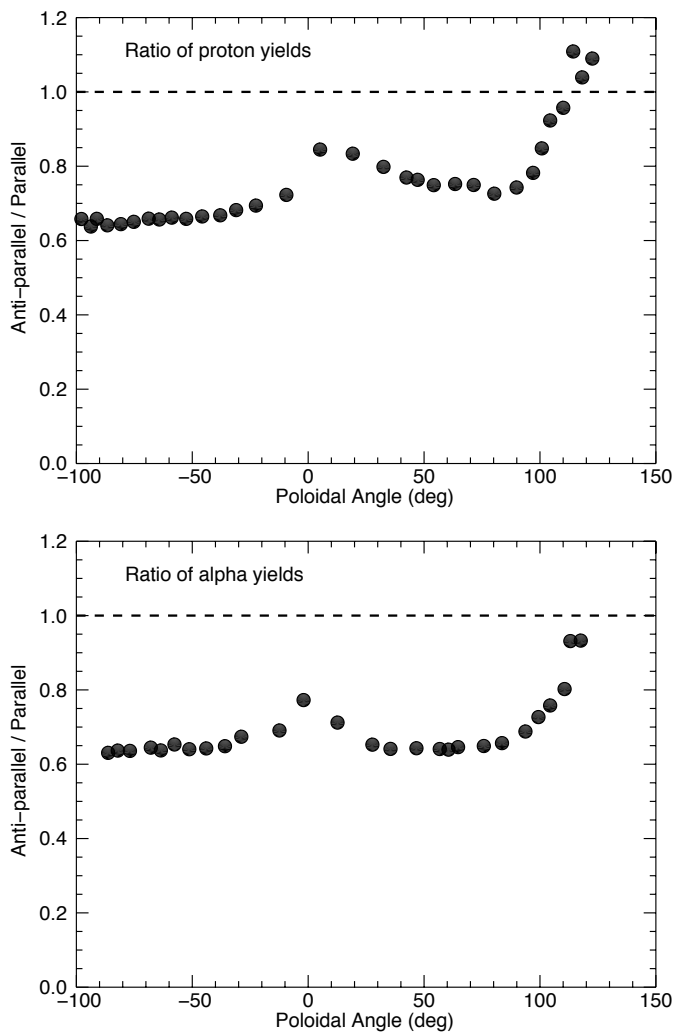

Figure 20. The predicted ratio of the high energy proton (top) and alpha (bottom) yields from successive plasma shots with D and 3He spins anti-parallel and parallel, for different locations along the plasma-facing wall of the DIII-D vacuum vessel, shown in terms of their poloidal angle.

unity extends well below the 0^0 mid-plane, the yields there are significantly smaller (figure 19). Thus, the existing DIII-D access ports at poloidal positions of 0°, 56°, 77° and 100° would be nearly optimum locations for particle detectors. If 70% vector-polarized deuterons were used (from ^{7}LiD pellets, as in S 5.1.2), these ratio profiles would be amplified significantly.

6.2 Requirements of plasma reproducibility

The DIII-D tokamak is a research-scale reactor with room temperature coils. Each *shot* is initiated with a 3 s ramp up to 2.1 Tesla, followed by a 10 s flat-field period in which ~80 keV neutral beams heat the plasma and measurements are carried out, and then a 7 s ramp down. There are then 15 min between shots to allow the coils to cool. To capitalize on the expected strong signals evident in figure 20 requires a comparison between multiple shots with very similar plasma characteristics.

A SPF demonstration experiment requires a hydrogen plasma, heated by neutral H beams, so as to avoid diluting the polarization of the reacting species. While a large number of plasma shots have been documented at DIII-D, the vast majority have been carried out with D-plasmas, heated by neutral D-beams. For a SPF study, the important metric is the product of ion density and temperature, integrated over the plasma volume and over the confinement time. This determines the thermonuclear reaction rate. However, in most archived D-plasma shots, reaction data is available only in the form of the neutron production rate, which is dominated by D-beam + D-plasma reactions during deuterium neutral beam injection; these occur at much higher energies where the cross section is at least an order of magnitude larger than in thermal reactions. (A review of past D+D experiments at DIII-D suggests a variability in the neutron production rate of less than 10% for plasmas with central ion temperatures of T_{ion} ~ 8 keV. This is chiefly a testimony to the stability of neutral beam injection.)

Fortunately, DIII-D is highly instrumented with diagnostics that monitor each plasma shot, and the operational parameter space has been well traveled. As an example, two successive plasma shots are shown in figure 2 of ref. [12], where ion current, electron temperature, the RMS amplitude of magnetic fluctuations, and electron density between the two shots are compared, and are clearly highly correlated. While H-plasmas heated with neutral H-beams will have to be

optimized for SPF, it is clear that the DIII-D diagnostics are available to characterize each plasma shot.

Most DIII-D shots have focused on D+D reactions, while past experience with hydrogen plasmas is limited. Furthermore, although the D+D cross sections change very rapidly at low energies (below about 8 keV – see figure 1), it is the high-T_{ion} range of 10 to ~25 keV that accounts for most of the thermonuclear yield, as in figure 2. Here the D+^{3}He fusion cross section is rising more rapidly than D+D, making the former more sensitive to changes in T_{ion} . At DIII-D, charge exchange recombination (CER) of carbon can be used to monitor T_{ion} [86], while CER of helium would provide the ^{3}He profile [87], and the main ion CER diagnostic would monitor the deuterium profile [88]. Optimizing a SPF experiment would be preceded by a systematic study to correlate plasma diagnostics with the thermonuclear fusion rates in proton and alpha detectors following the injection of unpolarized D pellets (^{7}LiD or HD) and unpolarized ^{3}He pellets. In this way, shots with comparable plasma conditions can be selected when comparing fusion yields from different fuel polarizations.

The number of shots required to verify the predictions of figure 20 will depend on the plasma variations one is willing to accept. A Monte Carlo simulation shows the effect of accepting larger shot variations for analysis. For a conservative estimate, the lower deuteron vector polarization of S 5.1.1 (40%) has been assumed here. The results are summarized in figure 21. With a pool of shots that have 8% systematic shot-to-shot variations in their fusion yields, a 5σ determination (the conventional criteria for "*discovery*") is obtained with merely four plasma shots in each spin orientation. Of course, it is not yet clear how many hydrogen plasma shots will be required

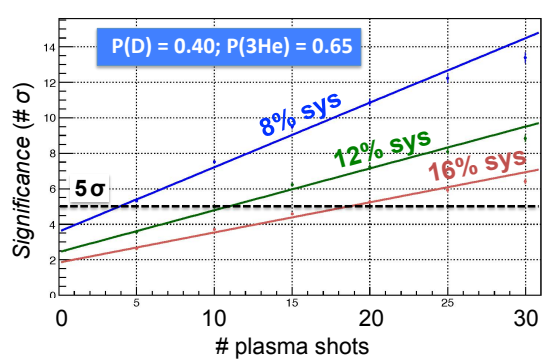

Figure 21. The number of plasma shots required to reach a given confidence level in terms of the statistical significance (σ), for different assumptions on the systematic shot-to-shot variations, as reflected in their fusion yields. The 5σ level for a definitive demonstration is indicated as the black dashed line.

before accumulating four in each spin orientation that have less than 8% plasma variations. It may prove easier to accept larger plasma variations; the effect of widening the criteria to 12% or 16% raises the required number of acceptable shots for a 5σ result to 11 or 18 in each spin orientation, respectively. For reference, DIII-D is capable of generating about 30 plasma shots per day, so this does not appear formidable.

An alternative approach to detecting polarization survival is discussed in a companion paper [23]. Simulations show that the pitch at the tokamak wall, taken as the arccos of the parallel component of the ion velocity $v_{\|} / v$, is strongly correlated with the polar reaction angle at birth. Since the dependence of the cross section on this angle is strongly polarization dependent, as in eg. (4) and Figure 5, the shape of the $v_{\|} / v$ velocity distribution at a fixed location on the tokamak wall also varies with polarization. Comparisons between shots with polarized and unpolarized fuel then reveal relative changes in the shape of fusion-product angular distributions, even if the plasma characteristics are appreciably different, as opposed to absolute rate measurements from similar plasma shots which are required for the ratios of figure 20.

6.3 Backgrounds from Secondary Reactions

In a $D + {}^3He \rightarrow \alpha + p$ polarization survival demonstration experiment, a hydrogen plasma should be used to avoid diluting the spins of the injected reactants. Nonetheless, a chain of parallel and secondary reactions can also lead to the production of alphas and protons. These are listed with their associated energy release (*Q values*) in eq. (12). Note that while triton production, followed by a subsequent $D + T$ reaction can generate an alpha of comparable energy to the $D + {}^3He \rightarrow \alpha + p$ fusion channel, the only secondary protons that are produced are low in energy and easily distinguished from those of the initial $D + {}^3He \rightarrow \alpha + p$ process.

$$\begin{aligned} {}^3He + D &\Rightarrow \alpha + p \quad (Q = +18.3 \text{ MeV}) \\ D + D &\Rightarrow {}^3He + n \quad (Q = +3.3 \text{ MeV}) \\ D + D &\Rightarrow T + p \quad (Q = +4.0 \text{ MeV}) \\ D + T &\Rightarrow \alpha + n \quad (Q = +17.6 \text{ MeV}) \end{aligned} \tag{12}$$

In principle, a dilution of the signal of interest can come from a two-step burn-up process [89], in which an initial reaction of two polarized deuterons produces a ^{3}He, the second process of eq. (12), with some transferred polarization that is less than that of the initial ^{3}He pellet and not generally aligned with the local field. However, the rate of the primary ^{3}He + D reaction providing the *signal* is simply proportional to the number of deuterons, *n(D)*, and for a hydrogen plasma, the density *n(D)* is just determined by the injected polarized fuel. The rate of the D + D reactions producing ^{3}He is proportional to $n(D)^2$, and the rate of the subsequent ^{3}He + D burn-up process is proportional to *n(D)*. Thus, the dilution of the signal of interest by the two-step burn-up process is quenched by the factor $n(D) / n(D)^3$, and so is essentially negligible.

7. Summary

Spin-polarized fuels can increase fusion reactivity by up to 50% and provide a significant boost towards the ignition of a burning plasma. In large-scale tokamaks, a further boost in power from increased alpha heating would accompany such gains. In the light of ITER simulations, it now seems quite likely that fuel polarization would survive through fuel burnup and have a major impact on performance (S. 3 and S. 4). A recent revolution in high-power lasers, combined with new molecular physics techniques, projects the capability of producing ~fully polarized D and T in the quantities needed for a fusion power reactor (S. 5.1.3). A necessary precursor to the research and development of such a capability is the crucial *in situ* demonstration of polarization survival in a high-T_{ion} plasma, and we have studied the key steps needed to execute such an experiment.

An experiment to test polarization survival can be carried out using the D+^{3}He $\rightarrow$ α+p reaction, avoiding the complications of handling tritium (S. 2). There have been significant developments in polarized materials over the last several decades, driven by nuclear and particle physics and by medical imaging. While their goals have been very different (*eg.* few mole samples with lifetimes of 10^5 to 10^8 s, whereas several kmoles per day would be needed to fuel a power reactor, but with mere ~10 s lifetimes), these existing techniques can be adapted to demonstrate an in-plasma spin enhancement in a cost-effective way. We have evaluated two options for preparing polarized deuterium, ^{7}LiD dynamically polarized to P_V^D = 70% (S. 5.1.1)

and frozen-spin HD polarized to P_V^D = 40% (S. 5.1.2). To deliver polarized deuterium, ^{7}LiD would require an 0.2 – 0.3 K polarizer that could transfer pellets to a nearby ~2 K injection gun; HD could be encapsulated in thin ICF shells, pre-polarized in another facility and loaded into a similar ~2 K injection gun. We have mapped out the characteristics of Glow-Discharge-Polymer (GDP) shells as a potential method of containing both HD and ^{3}He (S 5.1.2 and Appendix C). ^{3}He gas can be pre-polarized by laser optical pumping methods and then diffused into GDP shells. Leveraging advances in medical imaging, ^{3}He polarization loss during shell diffusion loading has been found to be relatively small (S. 5.2.1), and the polarization lifetime at 77 K unexpectedly long (S. 5.2.2). GDP shells of ^{3}He can be prepared with 65% polarization and delivered to a plasma with a ~77K injection gun. For the practical realization of such an experiment on DIII-D, a dedicated cryo-gun could be constructed to accommodate the injection of both polarized D and polarized ^{3}He through a vertical port (S. 5.3).

With a high T_{ion} hydrogen plasma, energetic protons (~15 MeV) detected at the plasma-facing wall would provide a nearly background-free monitor of D+^{3}He fusion (S. 6.3). The ratio of expected proton yields from successive plasma shots with D and ^{3}He spins parallel and anti-parallel range from 1.3 (HD + ^{3}He) to 1.6 (^{7}LiD + ^{3}He). Simulations of polarized fusion in a high-T_{ion} hydrogen plasma in the DIII-D tokamak have been carried out. Detailed tracking of fusion products confirms that this large signal is expected over a wide range of poloidal angles (S. 6.2). By correlating existing DIII-D plasma diagnostics with fusion rates from unpolarized D and ^{3}He, comparable plasma conditions could be selected to compare fusion yields from injected fuels with different spin alignments.

Acknowledgements

This work has been supported in part by the U.S. Department of Energy, Office of Science, Office of Nuclear Physics under contract DE-AC05-06OR23177, and under contracts DE-FC02-04ER54698 and DE-SC0020337. Support has also been provided by Internal Research and Development Funding from General Atomics, and in part by a grant from the University of Virginia Research and Initiative Fund. We thank G.M. Hale of LANL for carrying out the R-matrix analysis discussed in Section 2. We are indebted to M. Farrell, M. Hoppe and M. Schoff

of General Atomics for supplying ICF pellets for our test experiments, and to F. Li for her assistance with measurements of pellet dimensions at Old Dominion University. We thank T.P. Rakitzis of the University of Crete for many fruitful discussions on the potential for a new generation of laser-driven polarized sources (S. 5.1.3), M. Lanctot and H. St-John of General Atomics for their assistance with the ONETWO code used in the simulations of section 6.1, and C. Hanretty of Jefferson Lab for help with the Monte Carlo simulations shown in figure 21.

Appendix A. The D + $^3He^+$ angular distributions in their center of momentum frame

In the center-of-momentum frame (P_{total} = 0), the natural quantization axis is the local magnetic field direction, along which the approaching deuterium and ^{3}He spins will align, regardless of the angles of their initial-state momenta relative to the field direction. The reaction kinematics is shown schematically in figure A1.

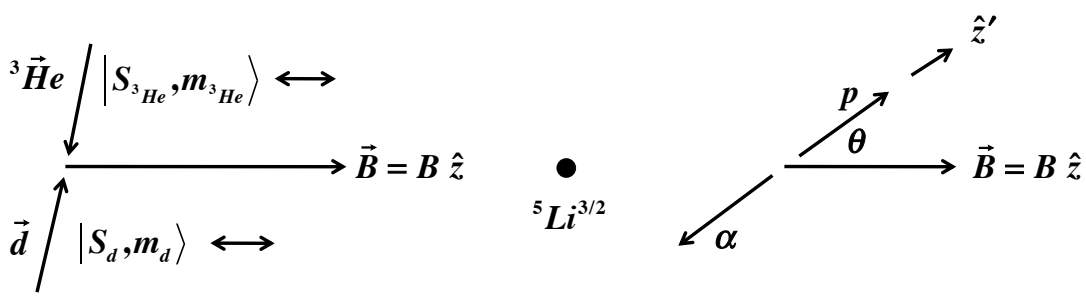

Figure A1. Initial (left) and final (right) states of the $d + {}^3He$ fusion reaction through a ^5Li compound state.

We calculate the angular dependence of the cross section for α-p decay through the 16.9 MeV spin 3/2$^+$ fusion resonance in ^{5}Li. With a Wigner-Eckart factorization, the reaction amplitude decomposes into a product of a reduced matrix element for fusion into the ^5Li intermediate state, a vector coupling (*Clebsch-Gordon*) coefficient for combining the d and ^3He spins along their initial direction ($\hat{z}$ in figure A1), another vector coefficient for coupling the final state spins along the α-p axis ($\hat{z}'$), and a Wigner $d^j_{m,m'}$ matrix element for the rotation between the two axes. Since the α has zero spin, to conserve parity and angular momentum, the α-p pair emerge from the spin (parity) *3/2* (+) compound state with two units of orbital angular momentum (*D-wave*, perpendicular to their momenta), as in figure 3. The cross section is then the squares of amplitudes, summed over allowed final states.

The cross section with d and ^3He spins both parallel (P) to the local field is then evaluated as,

$$\frac{d\sigma^P}{d\Omega} = \left|\left\langle f \middle\| T_{fi} \middle\| i \right\rangle\right|^2 \bullet \left|\left\langle 1+1;\tfrac{1}{2}+\tfrac{1}{2} \middle| \tfrac{3}{2}\ \tfrac{3}{2}\right\rangle\right|^2 \bullet \left\{ \left|\left\langle 2\ 0;\tfrac{1}{2}+\tfrac{1}{2} \middle| \tfrac{3}{2}+\tfrac{1}{2}\right\rangle\right|^2 \bullet \left|d^{J=3/2}_{3/2,\,+\frac{1}{2}}\right|^2 + \left|\left\langle 2\ 0;\tfrac{1}{2}-\tfrac{1}{2} \middle| \tfrac{3}{2}-\tfrac{1}{2}\right\rangle\right|^2 \bullet \left|d^{J=3/2}_{3/2,\,-\frac{1}{2}}\right|^2 \right\}$$

$$= \left|\left\langle f \middle\| T_{fi} \middle\| i \right\rangle\right|^2 \bullet \frac{2}{15} \bullet \left[\frac{9}{4}\sin^2\theta\right] \quad .$$

Similarly, when the *d* and ^3He spins are anti-aligned (*A*) relative to the local field,

$$\frac{d\boldsymbol{\sigma}^A}{d\boldsymbol{\Omega}} = \left|\left\langle f \left\| T_{fi} \right\| i \right\rangle\right|^2 \bullet \left|\left\langle 1+1;\tfrac{1}{2}-\tfrac{1}{2}\middle|\tfrac{3}{2}\ \tfrac{1}{2}\right\rangle\right|^2 \bullet \left\{ \left|\left\langle 2\ 0;\tfrac{1}{2}+\tfrac{1}{2}\middle|\tfrac{3}{2}+\tfrac{1}{2}\right\rangle\right|^2 \bullet \left|d^{J=3/2}_{1/2,\,+\frac{1}{2}}\right|^2 + \left|\left\langle 2\ 0;\tfrac{1}{2}-\tfrac{1}{2}\middle|\tfrac{3}{2}-\tfrac{1}{2}\right\rangle\right|^2 \bullet \left|d^{J=3/2}_{1/2,\,-\frac{1}{2}}\right|^2 \right\}$$
$$= \left|\left\langle f \left\| T_{fi} \right\| i \right\rangle\right|^2 \bullet \frac{2}{15} \bullet \left[\frac{1}{4}\left(1+3\cos^2\boldsymbol{\theta}\right)\right] \quad .$$

The unpolarized cross section for this reaction is isotropic, and can be constructed by averaging over all possible initial spin states. From this, the reduced matrix element can be recast as,

$$\left|\left\langle f \left\| T_{fi} \right\| i \right\rangle\right|^2 \bullet \frac{2}{15} = \left(\frac{d\boldsymbol{\sigma}}{d\boldsymbol{\Omega}}\right)_0 \quad .$$

Thus, the angular distributions with initial-state spins parallel and anti-aligned to the local field become,

$$\frac{d\boldsymbol{\sigma}^P}{d\boldsymbol{\Omega}} = \left(\frac{d\boldsymbol{\sigma}}{d\boldsymbol{\Omega}}\right)_0 \cdot \frac{9}{4} \cdot \sin^2\boldsymbol{\theta} \ \text{, and} \ \frac{d\boldsymbol{\sigma}^A}{d\boldsymbol{\Omega}} = \left(\frac{d\boldsymbol{\sigma}}{d\boldsymbol{\Omega}}\right)_0 \cdot \frac{1}{4} \cdot \left(1+3\cos^2\boldsymbol{\theta}\right) \ ,$$

which are the curves shown in figure 5. The full angular dependence given in eqn. (3a) can be derived in a similar manner. Thus, the highly anisotropic angular distributions that accompany the fusion of polarized fuel are a simple consequence of angular momentum and parity conservation.

Appendix B. Hyperfine splitting in singly-ionized $^3He^+$

The neutral ground state of ^{3}He has two electrons paired in a zero-spin *1s* state with no net effect on the nucleus. Following fuel injection, a plasma collision event strips away one electron in a time short compared to the state phase evolution (the sudden approximation). The system is then a $^3He^+$ ion with a hydrogen-atom-like state structure. There is a four-fold degenerate ground state of Coulomb and spin-orbit interactions that is split by the Zeeman interaction with the external field and the hyperfine interaction. While the Zeeman interaction with the external field ($J\,\mu B_z$) separately preserves the *m*-values of the ^{3}He nucleus and of the electron, the hyperfine

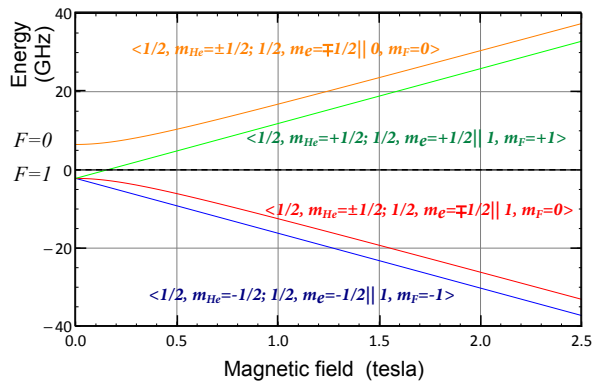

Figure B1. Eigen-energies in GHz of the $^3He^+$ ion as a function of external magnetic field, in Tesla. (For scale reference, 24 GHz ≡ 0.1 meV.) State mixing occures through the m_F =0 anti-symmetric (orange) and symmetric (red) hyperfine split states, respectively. The green and blue curves are for the states with both spins up and both spins down, respectively. See Reference [50].

interaction mixes them (A_{HFI} = -8.66565 GHz [50]). Diagonalizing the combined matrix gives the Eigen-energies of this 4-state system shown in Figure B1 as a function of external field. At zero field there are only two atomic states, with total angular momentum F = 0 or 1 and a separation determined by A_{HFI}. For non-zero field B, the F=1 states split into their three substate components. Mixing can occur between the m_F =0 substates; but this is strongly field dependent since, as evident in figure B1, above ~1 tesla the Zeeman splitting overwhelms the hyperfine splitting.

The calculation of the m_F =0 level mixing proceeds as follows. The sudden ionization to $^3He^+$ leaves the system in a state that can be described with the pure Zeeman basis states since it has a polarized nucleus with spin I and an un-polarized electron with spin S. The probability distribution in this basis is shown in column 3 of Table B1, for initial ^3He polarization P_0. These probabilities must then be projected onto the Eigen-states of the combined Zeeman and Hyperfine interactions to generate the probabilities shown in column 4, where a and b are the absolute values for the amplitudes of the major and minor Zeeman states in each mixed state. Note that $a^2+b^2=1$; $a=1/\sqrt{2}$ at zero field and a^2 ranges from 0.5 to 1. The four states then evolve in phase until the next collision, several milliseconds later, at which time all knowledge of their original phase is lost. The second ionization brings the system back to a pure Zeeman Eigen basis for nuclear spin only, since there are no electrons with which to interact. The projection of the mixed basis on to the pure Zeeman states is given in the last column of Table B1.

Table B1: Basis State Probabilities for an initial $^3He^+$ polarization P_0 .

m_S	m_I	Initial Pure Zeeman	Zeeman + Hyperfine	m_I	Final Pure Zeeman
+	+	$(1+P_0)/4$	$(1+P_0)/4$	+	$(1+P_0)/4$ $+a^2[a^2(1+P_0)/4+b^2(1-P_0)/4]$ $+b^2[a^2(1-P_0)/4+b^2(1+P_0)/4]$
+	-	$(1-P_0)/4$	$a^2(1-P_0)/4+b^2(1+P_0)/4$		
-	+	$(1+P_0)/4$	$a^2(1+P_0)/4+b^2(1-P_0)/4$	-	$(1-P_0)/4$ $+a^2[a^2(1-P_0)/4+b^2(1+P_0)/4]$ $+b^2[a^2(1+P_0)/4+b^2(1-P_0)/4]$
-	-	$(1-P_0)/4$	$(1-P_0)/4$		

The final polarization is the difference in the final state populations, from the last column of Table B1. The polarization loss simplifies to $\Delta P = -2a^2b^2P_0$, and the fractional loss becomes $\Delta P/P_0 = -2a^2(1-a^2)$. The mixing parameter "a" is field dependent and is determined by diagonalizing the 4 x 4 Zeeman+Hyperfine matrix. The net fractional polarization loss depends on the electron and ^3He magnetic moments, the strength of the hyperfine splitting and the magnetic field,

$$\frac{\Delta P}{P} = \tfrac{1}{2}\left[1+\frac{4(\mu_e-\mu_{ion})^2}{A_{HFI}^2}B^2\right]^{-1} . \qquad \text{(B1)}$$

Appendix C. Permeation characteristics of GDP shells

The Glow-Discharge-Polymer (GDP) shell material is commonly used in ICF experiments. Spheres are manufactured by vapor deposition onto the surface of poly-alpha-methylstyrene (PAMS) mandrels in a plasma of Trans-2 Butene and Hydrogen. Subsequent heating and pumping on the spheres removes the PAMS material, which permeates out and leaves behind a thin GDP shell comprised of a cross-linked structure of Carbon and Hydrogen. The C:H ratio can vary between 0.68 and 1.16, and higher values are associated with a higher Young's elastic modulus, making them more robust. Shells studied at JLab are typical of *standard* GDP shells,

with C:H ~ 0.85 and density 1.04 g/cc; these are the values used in the calculations of the extraneous particle numbers given in Table 2. The mechanical properties of GDP shells have been thoroughly investigated [18]. Their permeation characteristics relevant to this application have been studied at Jefferson Lab. Thin-walled shells are filled by controlling the temperature-dependent permeation rate. Initially, they are evacuated at room temperature by simply pumping on their storage container. The characteristic time constant (τ) when permeating an external pressure P_0 into an evacuated shell, $P_{GDP} = P_0(1 - e^{-t/\tau})$, depends linearly on shell dimensions, inversely on temperature and on a chemical permeation coefficient, $\tau = Dw/(6K_pRT)$ [90]. Here D is the diameter of the shell and w the wall thickness, the gas constant R is 8.314 m^3-Pa/mol-K, T is the temperature in Kelvin, and K_p is a permeation coefficient with an Arrhenius-type temperature-dependence, $K_p = K_0 \cdot exp(-\varepsilon_p / k_B T)$, expressed in units of mol/m-Pa-s, with a chemical activation energy ε_p (eV).

Sample pellets of about 2 mm diameter, with wall thicknesses between 14 and 29 microns, were supplied to JLab by GA. Precise measurements of pellet diameter and wall thickness were obtained, using facilities at *Old Dominion University*, by counting the interference fringes created when 546 nm monochromatic light passed through the pellet walls [91, 92].

Permeation measurements were carried out on a single pellet at a time. Each pellet was prepared at room temperature by evacuation within a small storage container, a stainless-steel tube with a 4 mm inside-diameter, and then filled with the gas of interest, allowing many permeation time constants at both steps. The measurements of permeation rates were then carried out following a sudden evacuation of the storage tube, to drop the pressure outside the pellet, and then subsequent monitoring of the rate of gas evolving with time from the container through either a Residual Gas Analyzer (RGA) or a leak detector (for gases of mass 3 or 4). Permeation measurements at elevated temperatures were carried out with the storage tube immersed in heated oil; for measurements at 273 K or 195 K the storage tube was immersed in baths of ice water or dry ice, respectively. The pressure from the gas permeating through the pellet wall (~ mb) was sufficient to maintain thermal equilibrium with the thermal bath.

As an example, the permeation rates measured through the 29 μm thick wall of a 1.9 mm diameter GDP pellet are plotted in figure C1 as a function of the square of the kinetic diameter of the gas species. Permeation is limited by the mean-free path in the material, which is in turn related to the cross-sectional area of the gas atom/molecule. This leads to a simple exponential

dependence, $exp(D^2/\alpha)$ where $\alpha \sim 2$ when D is expressed in Angstroms (*eg.* for the fits in figure C1, $\alpha = 2.045$). A change in temperature of the thermal bath by 75 degrees (C or K) leads to a parallel shift in permeation rates of all gases by a factor of 5. The permeation rates for the species relevant to the fusion experiment, with wall thicknesses ranging from 14 -to- 29 μm, are shown in figure 11 of section 5.1 over a larger temperature range. From the fit to those data (the dotted line in figure 11), the permeation coefficient is determined as K_o = 3.34 ±0.51 e-12 mol/m-s-Pa, with activation energy ε_p = 0.148 ±0.005 eV.

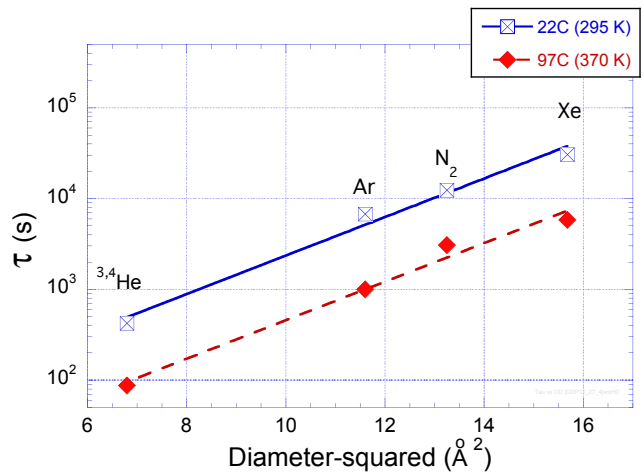

Figure C1. Permeation time constants measured at JLab for different gases in a 1.9 mm OD GDP pellet with a 29 μm wall thickness, at room temperature and at 97 C. (Statistical uncertainties are smaller than the symbols.)

Appendix D. MRI imaging of polarized ^{3}He shells

MRI relies on pulsed NMR in which nuclear spins, aligned along a static magnetic field, B_0, are subjected to pulses of an RF magnetic field, B_1, transverse to B_0, and oscillating at the nominal Larmor frequency $f_0 = \gamma B_0/2\pi$, where $\gamma/2\pi$ is the gyromagnetic ratio (-32.434 MHz/tesla for ^{3}He). Viewed semi-classically, an *excitation* RF pulse of flip angle θ tips a fraction $(1 - \cos\theta)$ of the aligned spins into the transverse plane. The transverse spins then precess about B_0 at the local Larmor frequency. The rotating magnetic field generated by the magnetic moments of the precessing spins induces an oscillating current in a surrounding RF receiver coil, which constitutes the NMR signal.

The amplitude for a signal generated by an RF excitation pulse, often referred to as the *Free Induction Decay* (FID*),* follows a decaying exponential of the general form, $S(t) = Ae^{i\phi}e^{-i2\pi(f-f_0)t}e^{-t/T_2^*}$. Here, f is the local resonance frequency, which can deviate from the Larmor frequency (f_0) due to chemical shifts induced by molecular bonds in surrounding material (or stray magnetic fields, if any), and T_2^* is the transverse spin relaxation time due to interactions with neighboring spins and local field inhomogeneities. If the sample contains more than one distinct spin population, each with its unique resonance frequency f_k, then the total signal is the coherent sum of multiple decaying exponentials, each with their own amplitude, phase offset, and transverse decay time. The frequency content of the FID can be resolved by taking the Fourier transform of the NMR signal. When the FID is a sum of decaying complex exponential functions, then its Fourier transform is a sum of complex Lorentzians.

Spatial localization in MRI is achieved by applying magnetic field gradients across the sample. The gradients, superimposed on B_0, cause the z component of the magnetic field to vary linearly along orthogonal directions, and this in turn causes the Larmor frequency to vary along those direction. Imaging data is acquired with an MRI *pulse sequence* - a prescribed series of RF pulses, magnetic field gradients, and data-sampling windows. These sequences use the linear mapping between frequency and position created by the applied gradients to encode spatial information about the excited spins into the frequency and/or phase of the NMR signal [93]. Signal data acquired in this manner are organized in terms of their Fourier-transformed coordinates - their "*k space*". For a study of polarization within 2 mm shells, we require half-millimeter imaging resolution, and for polarized gas this can be challenging. (Note that this is about an order of magnitude finer resolution than is typically of medical imaging with polarized gases.) We have achieved this with (fully *phase encoded*) pulse sequences that sample a single element of the *k*-space data matrix following each excitation RF pulse [77]. This takes advantage of the extremely long transverse decay time ($T_2^* \sim$ 100 ms) inside a hollow container [94], making it practical to enhance the signal-to-noise by longer signal readout times without decrementing polarization (ie. with low flip angle). Nonetheless, data over the entire field of view must be acquired to evaluate the k-space matrix. It is for this reason that the ^{3}He volume to be imaged is restricted to the small tubes of figure 12. This keeps the total time required for DAQ down to a manageable fraction of the pellet wall diffusion time so that the pellet permeation process can be directly observed.

The same pulse sequence can provide both spatial and spectral information. Applying a discrete inverse Fourier transform along the spatial dimensions transforms the *k*-space data into image space, and applying the Fourier transform along the temporal dimension yields the frequency spectrum of all transverse spins contained in each image pixel. The results are termed *Chemical Shift Images* (CSI), since discrete spin populations resulting from local magnetic field perturbations from chemical bond differences can be separated in frequency.

Immersing a uniform sphere in an otherwise uniform magnetic field creates a dipole-shaped field perturbation outside the sphere, whose overall magnitude scales with the magnetic susceptibility difference between the sphere and the surrounding medium [77]. This is the role of a solid glass bead positioned immediately beneath the GDP pellet, as evident in figure 12. The local magnetic field perturbation due to the nonzero magnetic susceptibility of the glass bead causes a small but prominent magnetic field shift inside the adjacent GDP pellet, and this allows the signal inside and outside the pellet to be tracked separately using spectrally sensitive CSI acquisition. (In fact, no such frequency separation is observed in experiments performed without the presence of a glass bead.)

Considering figure 13, all image voxels contain a spectral peak centered within a few Hz of the scanner's Larmor frequency, f_0. However, image voxels overlapping the location of the pellet also contain another prominent peak centered ~30 Hz above f_0. Because the ^{3}He diffusion length during the acquisition time exceeds the bead diameter, each spin can experience a wide range of frequency shifts across all voxels located within several millimeters of the glass bead. In contrast, the range of frequency shifts experienced by spins within the pellet is considerably narrower, because the pellet walls confine the encapsulated spins to a limited region of the dipole-shaped field perturbation. As a result, the NMR response of spins inside the pellet appear in a well-defined peak that is shifted in frequency [77, 78]. Thus, the frequency shifts resulting from the presence of the glass bead allow the NMR signal from spins located inside and outside the pellet to be tracked independently, providing separate time evolutions of each.

Appendix E. Orbit Tracking in DIII-D

The calculation for the flux of lost charged fusion products reaching the vessel wall consists of the following steps.

(1) Calculate the number of fusion reactions, F, as a function of major radius and elevation, $F = F(R_{birth}, z_{birth})$, where F is in units of particles/s. A radial profile of F is output by the ONETWO power balance code [85], and then distributed across a two-dimensional spatial grid in major radius and elevation to determine the particle starting locations.

(2) For each birth location featuring a non-zero fusion reaction rate, the number of fusion reactions is distributed across pitch angle and gyrophase:

- 13 values of pitch angle, $0^o \leq \theta \leq 180^o$, including $v_{\parallel}/v = \pm 1$,
- 12 values of gyrophase, excluding $v_{\parallel}/v = \pm 1$ (for which the gyrophase is singular).

An orbit is then calculated for each of these pitch angle and gyrophase pairs at each position (R_{birth}, z_{birth}). This is performed as the second step because identifying the values of (R_{birth}, z_{birth}) greatly reduces the number of orbits to be calculated.

(3) The orbit of each particle in (2) is calculated for 5000 steps with a 1 cm step size. If the particle does not hit the wall within 5000 steps, then it is considered to be confined. That number of steps is determined empirically and is considered reasonable because the large orbit scale of these high energy ions results in them reaching the wall very quickly unless their full orbit is confined (which is itself a very rare occurrence).

(4) In practice, with the discretization of step (2), each wall strike location originates from a unique birth location (R_{birth}, z_{birth}) with a specific choice of (pitch, gyrophase) angles. The particle flux at that wall location is determined by scaling the fusion rate $F = F(R_{birth}, z_{birth})$ from step (1) by the fraction of fusion products emitted into that (θ = pitch, ϕ = gyrophase) bin for the assumed degrees of fuel polarization, as determined by eq (4),

$$F'(R_{birth}, z_{birth}, \theta, \phi) = (1/4\pi)\, W_A(\theta)\, \sin(\theta)\, (\Delta\theta = \pi/13)\, (\Delta\phi = 2\pi/12)\, F(R_{birth}, z_{birth}) .$$

(5) Wall strikes are then histogrammed by binning the wall in segments of 0.01 m^2 in area (A). The particle count is reduced by a factor $2\pi R_i A$, where R_i is the major radius at the center of each wall segment, to account for the axisymmetry of the loss pattern. The end result is a particle flux density as a function of poloidal position along the wall, such as in figure 19.

References

[1] Conner J.P., Bonner T.W. and Smith J.R., 1952 *Phys. Rev.* **88**, 468
[2] Bonner T.W., Conner J.P. and Lillie A.B., 1952 *Phys, Rev.* **88**, 473
[3] Goldhaber M. 1934 *Proc. Cambridge Philos. Soc*. **30**, 561
[4] Kulsrud R.M., Furth H.P., Valeo E.J. and Goldhaber M. 1982 *Phys. Rev. Lett*. **49**, 1248
[5] More R.M. 1983 *Phys. Rev. Lett*. A **51**, 396
[6] Coppi B., Pegoraro, F. and Ramos J.J. 1983 *Phys. Rev. Lett*. **51**, 892
[7] Lodder, J.J. 1983 *Phys. Lett.* A**98**, 179
[8] Coppi B., Cowley S., Kulsrud R.M., Detagiache P. and Pegoraro, F. 1986 *Phys. Fluids* **29**, 4060
[9] Cowley S., Kulsrud R.M. and Valeo E.J. 1986 *E. J. Phys. Fluids* **29**, 1443
[10] Kulsrud R.M., Valeo E.J. and Cowley S. 1986 *Nucl. Fusion* **26,** 1443, and *references therein*
[11] Finn P., Brooks J., Ehst D., Gohar Y., Mattas R. and Baker C., *ANL/FPP*-85-1, *Report* DE86-007949; *ibid*, 1986 *Fus. Sci. Tech*. **10**, 902
[12] Pace D.C., Lanctot M.J., Jackson G.L., Sandorfi A.M., Smith S.P. and Wei, X. 2016 *J. Fus. Energy* **35**, 54
[13] Crabb D.G. and Meyer W., 1997 *Ann. Rev. Nucl. Part. Sci.* **47**, 67
[14] Goertz St., Meyer W., and Reicherz G., 2002 Prog. Part. Nucl. Phys. **49** 403
[15] Bass C.D. *et al*., 2014 *Nucl. Inst. Meth. Phys. Res.* A**737**, 107;
Lowry M.M. *et al*., 2016 *Nucl. Inst. Meth. Phys. Res.* A**815**, 31 and *references therein*.
[16] Babcock E., Nelson I., Kadlecek S., Driehuys B., Anderson L.W., Hersman F.W. and Walker T.G., 2003 *Phys. Rev. Lett*. **91**, 123003
[17] Mooney K.E., Miller G.W., Dolph P.A., Tobias W.A., Nelyubin V., Singh J., Mugler-III J.P. and Cates G.D., 2009 *Proc. Int. Soc. Mag. Reson. Med.* **17**, 2166
[18] Nikroo A., Czechowicz D., Castillo E. and Pontelandolfo J., 2002 *Fus. Sci and Tech.* **41**, 214;
Nikroo A., Czechowicz D., Chen K., Dicken M., Morris C., Andrews R., Greenwood A. and Castillo E., 2004 *Fus. Sci and Tech.* **45**, 229
[19] Baylor L.R., Jernigan T.C., Parks P.B., Antar G., Brooks N.H., Combs S.K., Fehling D.T., Foust C.R., Houlberg W.A. and Schmidt G.L., 2007 *Nucl. Fusion* **47**, 1598
[20] Sandorfi A.M. and D'Angelo A., in *Nuclear Fusion with Polarized Fuel*, 2016 *Springer Proc. Phys*. **187**, Springer-Verlag (*eds*. Ciullo G., Engels R., Büscher M. and Vasilyev A.) 115.
[21] Sandorfi A.M., Deur A., Hanretty C., Jackson G.L., Lanctot M., Liu J., Lowry M.M., Miller G.W., Pace D., Smith S.P., Wei K., Wei X., and Zheng X., *22nd Int. Spin Symp, (SPIN'16);* 2017 *arXiv:1703.06165v1.*
[22] Paetz gen. Schieck H., in *Nuclear Fusion with Polarized Fuel*, 2016 *Springer Proc. Phys*. **187**, Springer-Verlag (*eds*. Ciullo G., Engels R., Büscher M. and Vasilyev A.) 15.
[23] Garcia A.V., Heidbrink W.W., Sandorfi A.M., 2022 *Nucl. Fus.* (*in preparation*)
[24] Honig A. and Sandorfi A.M., Int. Spin Symp. 2006, 2007 *AIP Conf. Proc*. **915**, 1010
[25] Smith S.P., Sandorfi A.M., Pace D.C., Baylor L., Wade M., Miller G.W., Deur A., Liu J., Lowry M.M., Tafti S., Wei X., and Zheng X., 2019 *Proc. 27th IAEA Fusion Energy Conference*, https://nucleus.iaea.org/sites/fusionportal/Shared%20Documents/FEC%202018/fec2018-preprints/preprint0290.pdf
[26] Bosch H.-S. and Hale G.M. 1992 *Nucl. Fusion* **32**, 611
[27] Bahcall J.N., 1966 *Astrophys. J.* **143**, 259
[28] Aymar R., Barabaschi P. and Shimomura Y., 2002 ITER Design Rep*, Plasma Phys. Control. Fusion* **44**, 519
[29] Tilley, D.R., *et al.,* 2002 Nucl. Phys. A**708**, 3
[30] Hale G.M. and Dodder D.C., 1980 *NBS Spec. Publ*. **549**, 650
[31] Geist W.H., Brune C.R., Karwowski H.J., Ludwig E.J., Veal K.D. and Hale G.M., 1999 *Phys*. *Rev*. C**60**, 054003
[32] Lane A.M. and Thomas R.G. 1958 *Rev. Mod. Phys*. **30**, 257
[33] Hale G., LANL (2007 *private comm.*)
[34] Leemann CH., Bürgisser H., Huber P., Rohrer U., Paetz gen. Schieck H. and Seiler, F., 1971 *Ann*. *Phys*. **66**, 810
[35] Ohlsen G.G. 1972 *Rep. Prog. Phys*. **35**, 717

[36] Conzett H.E., *Proc. Tenth Int IUPAP Conf on Few Body Problems in Physics*, Karlsruhe, Germany, (Zeitnitz, B. *ed*) Elsevier Sci Publ. (1984) 539

[37] Rekalo M.P., and Tomasi-Gustafsson E. 1998 *Phys. Rev.* C**57**, 2870; *ibid* 2000 *arXiv:nucl-th*/0010046; *ibid* 2001 *arXiv:nucl-th*/0105007; *ibid* 2002 *Phys. Part. Nucl.* **33**, 220

[38] Garzotti L., Belo P., Corrigan G., Köchl F., Lönnroth J., Parail V, Pereverzev G., Saarelma S., Tardini G., Valovic M., Voitsekhovitch I. and Wiesen S., 2012 *Nucl. Fus.* **52**, 013002

[39] Ongena J., Evrard M. and McCune D., 2004 *Trans Fusion Science Technology* **45** 371; <theorycodes.pppl.wikispaces.net/TRANSP >

[40] Callen J.D., *Phys. Fluids* B 4 (1992) 2142

[41] Hölzl M., 2009 *Nucl. Fusion* **49**, 115009; Hölzl M., 2009 Technische Univ. München

[42] Belli E.A. and Candy J., 2015 *Plasma Phys. Control. Fusion* **57**, 054012; <fusion.gat.com/theory/Gyro>

[43] Hazeltine R.D., 1973 *Plasma Phys.* **15**, 77

[44] Staebler G.M., Kinsey J.E. and Waltz R.E., 2007 *Phys Plasmas* **14**, 055909; <fusion.gat.com/theory/Gyro>

[45] Candy J., Holland C., Waltz R.E., Fahey M.R. and Belli E., 2009 *Phys Plasmas* **16** 060704; <fusion.gat.com/theory/Gyro>

[46] Na Y.-S., 2006 *J Korean Phys Soc* **48** 576; 2008 *ibid* **53** 3788

[47] Lao L.L., St. John H.E., Peng Q., Ferron J.R., Strait E.J., Taylor T.S., Meyer W.H., Zhang C. and You K.I., 2005 *Fus. Sci. and Tech.* **48**, 968

[48] Burrell K.H., Kaplan D.H., Gohil P., Nilson D.G., Groebner R.J., and Thomas D.M., 2001 *Rev. Sci. Instrum.* **72**, 1028

[49] Carlstrom T.N., et al., 1992 *Review of Scientific Instruments* **63**, 4901

[50] Schuessler H.A., Fortson E.N., and Dehmelt H.G., 1969 *Phys Rev* **187**, 5 (1969); Erratum, 1970 *Phys. Rev.* **A2**, 1612

[51] Crampton S.B., Kleppner D., and Ramsey N.F., 1963 *Phys. Rev. Lett.* **11**, 338

[52] Wineland D.J. and Ramsey N.F., 1972 *Phys Rev* **A5**, 821

[53] Anderson L.W., Pipkin F.M. and Baird Jr J.C., 1960 *Phys. Rev.* **120**, 1279

[54] Bakalov D., Korobov V.I., and Schiller S., 2006 *Phys. Rev. Lett.* **97**, 243001

[55] Gatto R., in *Nuclear Fusion with Polarized Fuel*, Springer Proc. Phys., Springer-Verlag (eds. Ciullo G., Engels R., Büscher M. and Vasilyev A.) 2016 (*in press*)

[56] Pacher G.W., Pacher H.D., Janeschitz G. and Kukushkin A.S., 2008 *Nucl. Fus.* **48**, 105003

[57] Greenside H.S., Budny R.V. and Post D.E., 1984 *J. Vac. Sci Technol.* A **2**(2), 619

[58] Jackson G.L., Winter J., Taylor T.S., et al, 1991 *Phys. Rev. Lett.* **67,** 3098

[59] Jackson G.L., Winter J., Taylor T.S., et al, 1992 *Phys. Fluids* B **4,** 2181

[60] Pace D.C., Heidbrink W.W. and Van Zeeland M., 2015 *Physics Today* **68**, 34

[61] Coppi B., Cowley S., Kulsrud R., Detragiache P. and Pegoraro F., 1986 *Phys. Fluids* **29**, 4060

[62] McClements, K. G., D'Inca, R., Dendy, R. O., *et al*., 2015 *Nucl. Fusion* **55**, 043013

[63] Thome, K. E. *et al*., 2019 *Nucl. Fusion* **59** 086011

[64] Burrell K.H., Austin M.E., Brennan D.P., *et al*., 2002 *Plasma Phys. Controlled Fus.* **44**, A253; Burrell K.H., West W. P., Doyle E. J., Austin M. E., Casper T. A., Gohil P., Greenfield C. M., Groebner R. J., Hyatt A. W., Jayakumar R. J., Kaplan D. H., Lao L. L., Leonard A. W., Makowski M. A., McKee G. R., Osborne T. H., Snyder P. B., Solomon W. M., Thomas D. M., Rhodes T. L., Strait E. J., Wade M. R., Wang G., and Zeng L., 2005 *Phys. Plasmas* **12**, 056121.

[65] Bortolon A., Maingi R., Mans eld D.K., Nagy A., Roquemore A.L., Baylor L.R., Commaux N., Jackson G.L., Gilson E.P., Lunsford R., Parks P.B., Chrystal C., Grierson A., Groebner R., Haskey S., Makowski M.J., Lasnier C.J., Nazikian R., Osborne T., Shiraki D., and Van Zelland M.A., 2016 Nucl. Fusion **56** 056008.

[66] Abragam A., Bouffard V., Roinel Y., and Roubeau P., 1980 *J. de Physique Lett., Edp sciences* **41**, 309; Bouffard V., Roinel Y., Roubeau P., and Abragam A., 1980 *J. de Physique,* **41**, 1447.

[67] Wei X., Bass C.D., D'Angelo A., Deur A., Dezern G., Kageya T., Laine V., Lowry M.M., Sandorfi A.M., Teachey R.W., Wang H. and Whisnant C.S., 2013 *Proc. of Science* PoS (PSTP 2013))16

[68] Rakitzis T.P., *et al*., 2003 Science **300,** 1936.

[69] Rakitzis T.P., *et al*., 2005 *Phys. Rev. Lett.* **94,** 083005.

[70] Rubio-Lago L. *et al*., 2006 *Phys. Rev.* A**74**, 042503.

[71] Sofikitis D. *et al*., 2017 *Phys. Rev. Lett.* **118**, 233401;

Kannis C.S., Suarez J., and Rakitzis T.P., 2021 *Molecular Physics* **120**, e1975053; https://arxiv.org/pdf/2108.06133.pdf
[72] Kannis C.S., Rakitzis T.P., 2021 *Chem. Phys. Lett.* **784**, 139092
[73] Rakitzis T.P., 2019 (*priv. comm.*)
[74] Chen W.C. , Gentile T.R., Ye Q., Walker T.G., and Babcock E., 2014 *J. Appl. Phys.* **116**, 014903.
[75] Jacob R.E., Morgan S.W., Saam B. and Leawoods J.C., 2001 *Phys. Rev. Lett.* **87**, 143004
[76] Farrell M., Hoppe M. and Schoff M., *priv. comm.*
[77] Tafti S., *Magnetic Resonance Imaging of Spin-Polarized ^{3}He and ^{129}Xe*, 2020 *Univ. of Virginia thesis*, https://doi.org/10.18130/v3-h4e5-4t97 .
[78] Tafti S., Liu J., Sandorfi A.M., Wei K., Wei X., Zheng X., and Miller G.W., 2022 *Nature-Phys.* (*submitted*)
[79] Scaling experiences at JLab and the University of Virginia with [surface/volume]$^{-1}$ and [pressure]$^{-1}$ projects T_1 ~ 125 hr, although relaxation times up to 450 hr in ~1 liter volumes have been reported in ref [74].
[80] Reynolds H., Baxamusa S., Haan S.W., Fitzsimmons P., Carlson L., Farrell M., Nikroo A., and Watson B.J., 2016 *J. Appl. Phys.* **119**, 085305
[81] Zheng X., *et al.*, 2004 *Phys. Rev. C* **70**, 065207
[82] Hollmann E.M., (*priv. comm.*)
[83] Chen X., Fisher R.K., Pace D.C., Garcia-Munoz M., Chavez J.A., Heidbrink W.W., and Van Zeeland M.A., 2010 *Rev. Sci. Instrum.* **83**, 10D707
[84] Duong H.H., and Heidbrink W.W., 1993 *Nucl. Fusion* **33**, 211
[85] Pfeiffer W.W., Davidson R.H., Miller R.L. and Waltz R.E., *ONETWO: A computer code for modeling Plasma Transport in Tokamaks*, 1980 *General Atomics Report* GA-16178;
St. John H., Taylor T.S., Lin-Liu Y.R. and Turnbull A.D., 1995 *Proc. 15th Int Conf on Plasma Physics and Controlled Nuclear Fusion Research*, IAEA-CN-60/D-P22, **3**, 603.
[86] Chrystal C., Burrell K.H, Grierson B.A., Haskey S.R., Groebner R.J., Kaplan D.H., and Briesemeister. A., 2016 *Rev. Sci. Instrum.* **87**, 11E512
[87] Wade M.R., Hillis D.L., Hogan J.T., Maingi R., Menon M.M., Mahdavi M.A., West W.P., Burrell K.H., Gohil P., Groebner R.J., *et al.*, 1995 *Phys. of Plasmas* **2**, 2357
[88] Haskey S.R., Stagner L., Grierson B.A., Chrystal C., DeGrandchamp G.H., Heidbrink W.W., Van Zeeland M.A., and Vincena S., 2021 *Rev. Sci. Instrum.* **92**, 043535
[89] Heidbrink W.W., Chrien R.E., and Strachan J.D., 1983 *Nucl. Fusion* **23**, 917
[90] Scott L.A., Schneggenburger R.G., and Anderson P.R., 1986 *J. Vac. Sci. Technol*. **A4**, 1155;
Tsai F.Y., Blanton T.N., Harding D.R., and Chen S.H., 2003 *J. Appl. Phys.* ***93***, 3760
[91] Prasad M.K., Estabrook K.G., Harte J.A., Craxton R.S., Bosch R.A., Busch Gar.E., and Kollin J.S., 1992 *Phys. Fluids* ***B4***, 1569; see also Laboratory for Laser Energetics, 1995 *LLE Review*, **64**, 175
[92] Craxton R.S. (*ed.*), 1995 *LLE Review* ***64, 175; OSTI.GOV***: https://doi.org/10.2172/171363 .
[93] M.A. Bernstein, K.F. King and X.J. Zhou, *Handbook of MRI Pulse Sequences*, Academic Press (2004); https://doi.org/10.1016/B978-0-12-092861-3.X5000-6 .
[94] Zheng Y., Cates G.D., Mugler III J.P., Tobias W.A., and Miller G.W., 2014 *J. Magn. Reson.* **249**, 108.